Article

Exceptional Preservation of Fungi as H₂-Bearing Fluid Inclusions in an Early Quaternary Paleo-Hydrothermal System at Cape Vani, Milos, Greece

Magnus Ivarsson [1,2,*], Stephanos P. Kilias [3], Curt Broman [4], Anna Neubeck [5], Henrik Drake [6], Ernest Chi Fru [7], Stefan Bengtson [2], Jonathan Naden [8], Kleopatra Detsi [3] and Martin J. Whitehouse [9]

[1] Department of Biology, University of Southern Denmark, Campusvej 55, 5230 Odense, Denmark

[2] Department of Paleobiology, Swedish Museum of Natural History, Box 50007, 10405 Stockholm, Sweden; stefan.bengtson@nrm.se

[3] Department of Economic Geology and Geochemistry, Faculty of Geology and Geoenvironment, National and Kapodistrian University of Athens, Panepistimiopolis, Zographou, 15784 Athens, Greece; kilias@geol.uoa.gr (S.P.K.); detsi@geol.uoa.gr (K.D.)

[4] Department of Geological Sciences, Stockholm University, SE-10691 Stockholm, Sweden; curt.broman@bredband.net

[5] Department of Earth Sciences, Uppsala University, SE-75236 Uppsala, Sweden; anna.neubeck@geo.uu.se

[6] Department of Biology and Environmental Science, Linnæus University, 392 31 Kalmar, Sweden; henrik.drake@lnu.se

[7] School of Earth and Ocean Sciences, Institute for Geobiology and Geochemistry, Cardiff University, Park Place, Cardiff CF10 3AT, UK; chifrue@cardiff.ac.uk

[8] British Geological Survey, Keyworth, Nottingham NG12 5GG, UK; jna@bgs.ac.uk

[9] Department of Geosciences, Swedish Museum of Natural History, Box 50007, SE10405 Stockholm, Sweden; martin.whitehouse@nrm.se

* Correspondence: magnus.ivarsson@nrm.se

Abstract: The production of H₂ in hydrothermal systems and subsurface settings is almost exclusively assumed a result of abiotic processes, particularly serpentinization of ultramafic rocks. The origin of H₂ in environments not hosted in ultramafic rocks is, as a rule, unjustifiably linked to abiotic processes. Additionally, multiple microbiological processes among both prokaryotes and eukaryotes are known to involve H₂-production, of which anaerobic fungi have been put forward as a potential source of H₂ in subsurface environments, which is still unconfirmed. Here, we report fungal remains exceptionally preserved as fluid inclusions in hydrothermal quartz from feeder quartz-barite veins from the Cape Vani Fe-Ba-Mn ore on the Greek island of Milos. The inclusions possess filamentous or near-spheroidal morphologies interpreted as remains of fungal hyphae and spores, respectively. They were characterized by microthermometry, Raman spectroscopy, and staining of exposed inclusions with WGA-FITC under fluorescence microscopy. The spheroidal aqueous inclusions interpreted as fungal spores are unique by their coating of Mn-oxide birnessite, and gas phase H₂. A biological origin of the H₂ resulting from anaerobic fungal respiration is suggested. We propose that biologically produced H₂ by micro-eukaryotes is an unrecognized source of H₂ in hydrothermal systems that may support communities of H₂-dependent prokaryotes.

Keywords: fungi; hydrothermal system; molecular hydrogen

1. Introduction

Hydrothermal systems are recognized as environments of remarkable microbiological diversity and abundance [1]. With respect to exploration of microbiological communities, most efforts have been on prokaryotes, whereas eukaryotes have been largely overlooked. The few studies devoted to eukaryotes indicate a notable diversity including fungi, green algae, animals, as well as alveolates, of which a previously undescribed majority are representatives of early branching eukaryotic lineages [2–5]. Most of the investigations have been performed either on shallow-water sediments at vent sites or on hydrothermal fluids dissipating directly from vents. Deeper in the underlying rocks, our knowledge of the eukaryotic abundance and diversity is still poor. Fungi are so far the only eukaryotes that have been isolated from subseafloor basalts [6]. A recently discovered fossil record in subseafloor crust indicates that fungi are, in fact, abundant and widely distributed spatially, and with depth and age [7–9]. The presence of fungi in such deep and remote environments raises questions regarding their metabolism and ecological role [8,10,11]. Fungi are known from other environments, like soils, to play a crucial role in biogeochemical cycles and symbiotic relationships with other organisms [12,13]. Observations from the fossil record suggest fungi to play a similar role in the oceanic crust, where they are involved in mineral weathering and precipitation, decomposition of organic matter, and engage in symbiotic-like relationships with chemoautotrophic prokaryotes [7,14–16].

The majority of the subseafloor environments from which eukaryotes, including fungi, have been detected or isolated, are anoxic or suboxic in nature. A facultative or obligate anaerobic nature is by implication inferred for the eukaryotes living in these environments, but the physiological and ecological implications are seldom recognized and discussed [2]. Facultative anaerobic fungi occur among all fungal phyla, but obligate anaerobic fungi are only known from the Phylum Neocallimastigomycota, which almost exclusively are known from rumens of ruminant herbivores [17,18]. A majority of fungi from deep-sea settings belong to Ascomycota or Basidiomycota or are undescribed [5], thus not belonging to the Neocallimastigomycota, and implying that there seems to be fundamental gaps in our knowledge regarding deep fungi and their metabolism. Obligate eukaryotes, including Neocallimastigomycota, have hydrogenosomes instead of mitochondria, which evolve H_2 during respiration [17,18]. In rumens, the fungal growth is inhibited by the presence of H_2; however, the fungi exist in intimate symbiosis with H_2-consuming methanogens and acetogens [19,20]. The fungal–prokaryotic symbiosis stimulates growth of both partners. A similar symbiotic relationship between anaerobic fungi and H_2-dependent prokaryotes was hypothesized to be functional and vital in anoxic subseafloor environments [21]. The presence of fossilized fungal hyphae and syngenetic pyrite with $\delta^{34}S$ signatures indicating bacterial sulfate reduction corroborated such a partnership in strictly anoxic fractures at >700 m depth in the Swedish crystalline basement [22]. Yet, confirmation of H_2-producing fungi in subsurface and subseafloor environments would strengthen this hypothesis and expand the ecological role of anaerobic eukaryotes in deep biosphere settings.

Molecular hydrogen is the fundamental energy source for deep-biosphere lithoautotrophic communities [23–26] and is assumed to be predominantly produced abiotically by mineral–fluid interactions, radiolysis, or originate from volcanic gases [24]. The highest fluxes of H_2 are found in serpentine hosted environments owing to the abiotic production of H_2 during serpentinization [27]. Otherwise, the rates of H_2 production are low, even in basalt hosted systems [28]. It has been questioned whether abiotic processes in environments other than serpentine hosted systems can form H_2 in sufficient amounts to sustain lithoautotrophic communities [29]. For instance, deep groundwater (down to 1000 m depth) from the Fennoscandian shield shows highly variable H_2 concentrations that are correlated neither with depth nor with residence times of the waters, which implies that radiolysis is not the sole source of the elevated H_2 concentrations [22]. In addition to abiotic production of H_2, biological production may occur in anoxic to suboxic environments by bacterial fermentation [1]. However, biological production of H_2 is rarely regarded as an important contributor to the main H_2 pool [30]. Besides, biologically produced H_2 is almost always considered

to be produced by bacteria [1]. Eukaryotes are rarely accounted for, but a confirmation of eukaryotic H_2 production would challenge the present notion of biological H_2 in natural environments.

In remote and extreme environments, like the oceanic crust and hydrothermal systems, where sampling of live specimens is difficult, fossilized material has been used as an alternative approach to study microorganisms and microbial consortia [7]. Hydrothermal environments are characterized by rapid mineral growth, which fosters instant entombment and fossilization of microorganisms and, thus a high grade of preservation. Fossilized consortia have the advantage of usually being easier to visualize in three dimensions than live microbial communities. The spatial relationship between prokaryotes and eukaryotes has been visualized [14], and differentiation between prokaryotes and eukaryotes including various types of fungi has been shown by detailed morphological studies of fossilized material [7].

Here we report fossilized fungi, exceptionally preserved as fluid inclusions, in a paleo-hydrothermal system associated with Mn-ore on Milos island, Greece. We combine results from biochemical staining, fluid-inclusion microthermometry, and Raman spectroscopy with microscale and bulk sample stable isotope analysis of the mineral phases to describe the putative fossils, related mineralogy and the environment in which the organisms lived. The fossil imprints display characteristic fungal features and contain H_2 as gas phase. We suggest fungi as producers of H_2 in subseafloor hydrothermal environments, although the evaluation of the quantities and their geobiological impact remains.

1.1. Geology and Mineralization of Milos

The Milos Island is a recently emerged volcanic edifice of the Pliocene–modern Hellenic volcanic arc (HVA), Greece. It comprises Upper Pliocene submarine and Upper Pleistocene to Holocene submarine-to-subaerial calc-alkaline volcanic domes, lavas, and pyroclastic deposits consisting of andesites, dacites, and rhyolites [31,32]. Volcanism was constructed on a Mesozoic basement and Miocene–Pliocene marine sediments representing a transition from shallow submarine to subaerial volcanic environments [31,32]. Milos hosts a range of mineralization from polymetallic massive sulfides to vein-style precious metals considered as analogs for mineralization in volcanic arcs that is continuous across the submarine-subaerial transition [33–36].

The Cape Vani sedimentary basin (CVSB), NW Milos, is a sedimentary rift basin, floored by dacitic–andesitic lava domes and overlain by Lower Pleistocene fossiliferous volcaniclastic sandstone/sandy tuff infill [31,32,37–39]. It hosts a fossil analog of active shallow submarine hydrothermal activity on the Milos coast [40]. The CVSB has been divided into three lithologically variable, fault-bounded volcano-sedimentary sub-basins [39]: (A) Basin 1, host of microfossil-rich Precambrian banded iron formation (BIF)-type deposits (MFIF); (B) Basin 2, host of economic-grade Mn oxide ores; and, (C) Basin 3, host of non-fossiliferous BIF-type deposits (NFIF) (Figure 1). Most of the CVSB volcaniclastics hosting the Mn-rich deposit are foreshore to shoreface shallow submarine deposits [37,38,41]. The BIF-type deposits are considered Earth's youngest BIF analogs of Quaternary age [39].

The well-preserved hydrothermal Fe-Ba-Mn deposit is hosted by unmetamorphosed fossiliferous Lower Pleistocene volcaniclastic sandstones/sandy tuffs, which are underlain by submarine dacitic-andesitic lava domes (Figure 1) [31,32,37–39]. Quartz-barite (Mn oxide, chalcedony, K-feldspar) hydrothermal feeder veins cut the entire section. The Mn oxide ores typically construct texturally diverse cements to a variety of volcaniclastic detritus and authigenic mineral grains. The Mn-oxides consist of pyrolusite and ramsdellite as an early generation, cryptomelane-hollandite-coronadite together with hydrohetaerolite as a second generation, as well as barite formed throughout the duration of Mn oxide mineralization at Cape Vani [37,38]. In the deposit, barite occurs as

(i) disseminated crystals or cement in Mn-mineralized sandstone/sandy tuff;

(ii) quartz-barite (chalcedony, Mn oxide, K-feldspar) hydrothermal veins showing epithermal textures. These occur throughout the stratigraphy, crosscutting both the

dacite/andesite basement and the overlying Mn-mineralized sediments, where they become more rich in barite and Mn-oxide;

(iii) bedding-conformable barite (±Mn oxide, silica)-rich horizons underlain by mineralogically similar discordant pipe-like bodies; and

(iv) barite-rich white smoker-like paleo-seafloor structures [37,41–43].

These hydrothermal quartz- and barite-rich deposits are closely associated with Mn-mineralized, bedding-concordant microbial mat-related sedimentary structures [41]. The Mn deposit is interpreted as synvolcanic shallow-marine/tidal-flat seafloor and subseafloor, which exhibits a range of seafloor-exhalative, subseafloor-replacement and infilling, stratiform and stratabound layers, as well as structurally controlled stringer network styles [37,38,41,44].
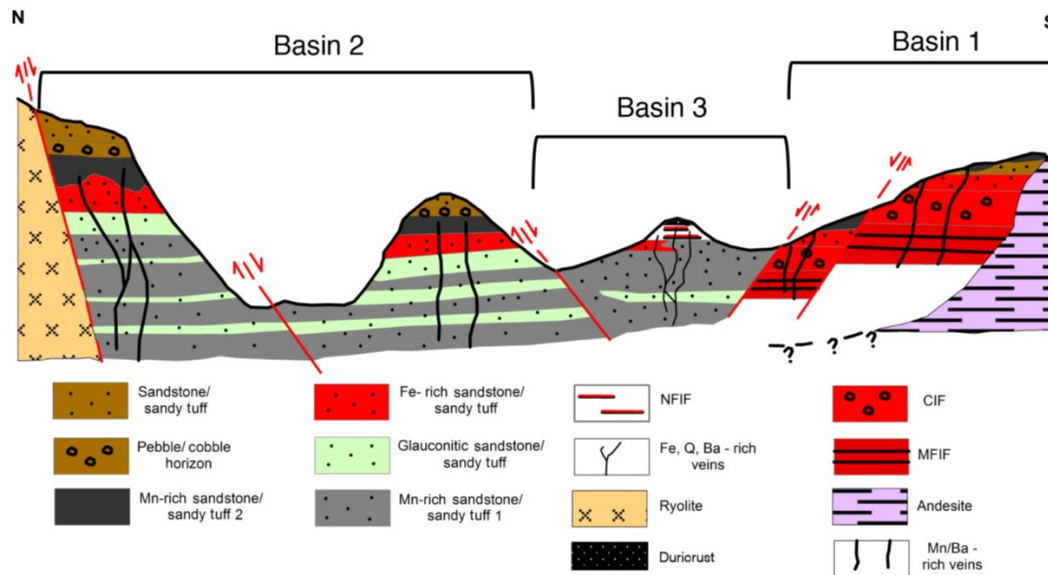

Figure 1. A generalized north-south stratigraphic map of the ~1 km long the Cape Vani sedimentary basin (CVSB) showing interpreted geology, lithology, and main faults. CIF: conglomerate-hosted iron formation; NFIF: nonfossiliferous iron formation; MFIF: microfossiliferous iron formation.

2. Materials and Methods

Our study used the geologic and stratigraphic knowledge delineated by previous studies (see Figure 1) [37–39,41–43,45]. Samples were mostly collected from Basin 2 outcrops inside the abandoned Cape Vani Mn mine, where they are either from veins (n = 7) volumetrically dominated by coarse-bladed massive barite set in an amorphous silica and crystalline quartz matrix (Figure 2A), or from cavity fillings and cement of sandstone (n = 3) (Figure 2B,C). To supplement this material, samples were also collected from stockwork veins stratigraphically below the mine; these veins have typical epithermal crustiform banded textures and consist of coarsely crystalline and zoned barite bands separated by massive, colloform, and comb quartz (Figure 2D).

The samples were prepared as doubly polished thin sections (~150 μm thick) and investigated by optical and fluorescence microscopy, microthermometry, and Raman spectroscopy to identify and characterize mineralogy, fluid inclusions, and microbial morphologies. Stable C, S, and O isotopes were analyzed for the mineral material, both for bulk sample material and microscale within individual barite crystals.
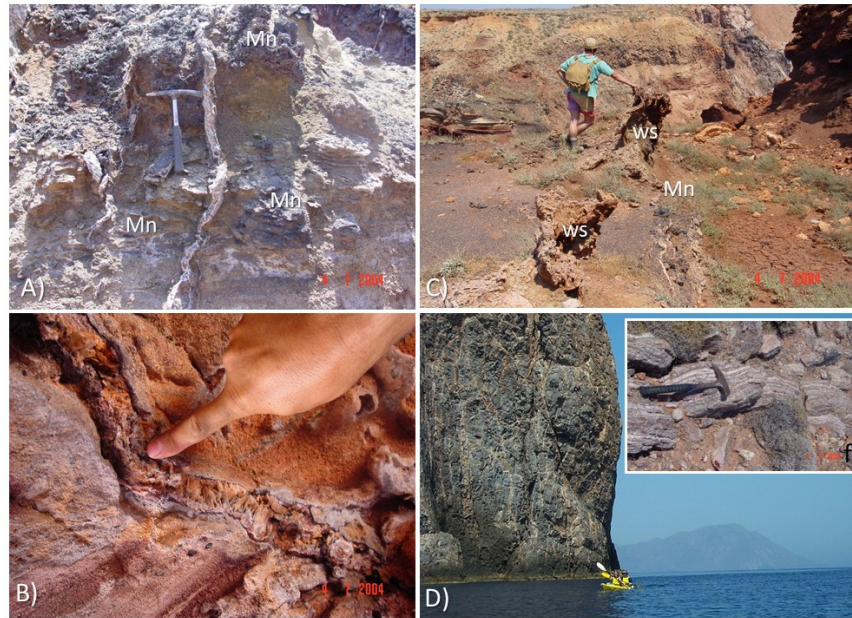
Figure 2. (**A**) Epithermal, discordant to bedded sandstone, quartz-barite (chalcedony, Mn oxide) veins within the Cape Vani abandoned open pit Mn mine. The vein comprises, narrow margin of finely crystalline chiefly barite bands, and coarse bladed "comb" barite intergrown with quartz-chalcedony as central vein infill. Note manganese mineralization that occurs as thin layers, encrustations, and cement of sandstone (Mn). (**B**) Euhedral barite laths preserved in barite-rich open space filling texture, Cape Vani Mn mine. (**C**) Steep, bifurcating curvilinear vein swarms which project to barite(-silica)-rich white smoker-like structures (WS), and Mn encrustations (Mn) characteristic of seafloor venting. (**D**) Steeply dipping almost vertical stockwork veins, below the mine level, that represent fluid feeder structures to the Cape Vani basin, crosscut the underlying lavas and hyaloclastite for several tens of meters below the epiclastic/volcaniclastic sediments. These feeder veins show typical epithermal crustiform banded quartz-barite textures. Inset: Plan view of outcrop of typical epithermal crustiform–colloform veins.

2.1. Microthermometry

Representative vein samples were taken from the underlying dacitic–andesitic lavas and hyaloclastite below the mine level (Figure 2D), to the near- and sub-paleoseafloor volcaniclastic sediments, including material immediately adjacent to structures analogous to modern-day white smokers characteristic of seafloor venting (Figure 2B,C), and microbial-mat related sedimentary structures [41]. The analyses were made at the Department of Economic Geology and Geochemistry; National and Kapodistrian University of Athens (NKUA); and the Department of Geological Sciences, Stockholm University. A conventional microscope was used to get an overview of the distribution of fluid inclusions. Microthermometric measurements on fluid inclusions in barite and quartz were performed with a Linkam THM 600 stage mounted on a Nikon microscope utilizing a 40x long working-distance objective. The working range of the stage is −196 °C to +600 °C. Calibration was made using SynFlinc® synthetic fluid inclusions and well-defined natural inclusions in Alpine quartz. The reproducibility was ±0.1°C for temperatures below 40 °C and ±0.5 °C for temperatures above 40 °C.

2.2. Raman Spectroscopy

Raman spectra were collected at the Department of Geological Sciences, Stockholm University, using a confocal laser Raman spectrometer, Horiba instrument LabRAM HR 800; Horiba Jobin Yvon, equipped with a multichannel air-cooled (−70 °C) 1024 × 256 pixel CCD (charge-coupled device) detector. Acquisitions were obtained with an 1800 lines/mm grating. Excitation was provided by an

Ar-ion laser (λ = 514 nm) source. Raman spectra were recorded in the 150–4300 cm^{-1} region and were obtained under weak laser excitation power (0.1 to 1 mW) at the sample surface to alleviate any decomposition of the samples. The sample material was placed on a glass slide on an Olympus BX41 microscope coupled to the instrument. The laser beam was focused through a 100x objective to obtain a spot size of about 1 μm. Collection times for the Raman spectra are 10 accumulations of 5 s each. The accuracy of the instrument was controlled by repeated use of a silicon (Si) reference with a Raman line at 520.7 cm^{-1}. The Raman spectra were collected using the LabSpec 5 software.

2.3. Staining with WGA-FITC and Fluorescence Microscopy

Thin sections were stained with WGA-FITC (Sigma-Aldrich lectin from Triticum vulgaris FITC conjugate) according to the method in [46]. All samples were examined by fluorescence microscopy before incubation with WGA-FITC to exclude native fluorescence in the regions of interest, and controls were made to exclude the possibility of WGA-FITC binding to minerals in the thin sections. Fluid inclusions close to the thin section surface were chosen and subjected to laser excitation power (1 > mW) by Raman spectroscopy to penetrate the sample surface and expose the fluid inclusion interior and content prior to the staining procedure. The samples were washed three times with distilled water (10 min each wash) prior to exposure and incubation with WGA-FITC, which lasted for 2 h. The concentration of the lectin in the incubation medium was 50 μg/mL in 10 mmol/L phosphate buffer. After incubation the samples were washed three times with distilled water and examined under fluorescence microscope. A Leitz DMRBE epifluorescent microscopy equipped with a Leica DFC 280 camera was used.

2.4. Stable Isotopes

Stable isotope compositions of C and S were determined on bulk quartz-barite samples that contain hydrocarbon inclusions. There were no carbonates or hydrocarbons in the samples other than in the fluid inclusions. The stable isotope measurements were determined at the Stable Isotope Laboratory at the Department of Geological Sciences, Stockholm University. The samples were hand-ground to a fine powder with a sterilized (95% ethanol) agate mortar and pestle prior to combustion with a Carlo Erba NC2500 analyzer connected, via a split interface to reduce the gas volume, to a Finnigan MAT Delta plus mass spectrometer. From these measurements, the reproducibility was calculated to be better than 0.15‰ for δ^{13}C. The relative error was <1% for all measurements.

Barite stable isotope analyses (δ^{34}S and δ^{18}O) were undertaken at the Scottish Universities Environmental Research Centre using the techniques of [47,48]. For sulfate sulfur analyses, SO_2 gas was liberated by combustion with excess copper (I) oxide and silica at 1125 °C. Gases were analyzed on a VG Isotech SIRA II mass spectrometer, and standard corrections applied to raw $\delta^{66}SO_2$ values to produce true δ^{34}S. International standards NBS-123 and IAEA-S-3, and the SUERC standard CP-1 gave δ^{34}S values of +17.1‰, −31‰, and −4.6‰, respectively, with 1σ reproducibility better than ±0.2‰. Data are reported in δ^{34}S notation as per mil (‰) variations from the Vienna Cañon Diablo Troilite (V-CDT) standard. For sulfate oxygen analyses, barite was carefully cleaned by washing and rinsing in Aqua Regia, and deionized water. Oxygen was extracted by heating barite and graphite to 1200 °C and the evolved carbon oxides converted to CO_2 and C by reduction in a Pt-electrode, high-voltage (2 kV) discharge vessel held at liquid nitrogen temperature. The CO_2 was then analyzed on a VG Sira 10 mass spectrometer, with all results reported in standard delta notation as ‰ variations relative to the V-SMOW international standard. Replicate analyses of the NBS-127 $BaSO_4$ standard during these analyses gave +9.6 ± 0.3‰.

Stable S and O isotopes in barite were also determined within single crystals using a Cameca IMS1280 secondary ion mass spectrometry (SIMS) at NordSIM facility, Stockholm, Sweden. Two to four crystals (mainly two) were analyzed from four samples (BD-14, 15, 16, 17), and up to ten analyses were made for each crystal, in transects from inner growth zone to rim, with closely spaced analyses for S and O isotopes, with a higher number of analyses for O (n = 96) than for S (n = 40). Separate analytical routines applied for S and O, are described briefly below, and closely follow those described in [49] for sulfur, with the exception that only ^{34}S/^{32}S ratios were measured here, and in [50]

for oxygen. For both elements, the samples were sputtered using a Gaussian focused $^{133}Cs^+$ primary beam with 20 kV incident energy (10 kV primary, −10 kV secondary) and primary beam current of ~3 nA, which was rastered over a 5 μm × 5 μm area during analysis to homogenize the beam density. The resulting analytical crater had a diameter of ~10 μm. A normal incidence electron gun was used for charge compensation. Analyses were performed in automated sequences, with each analysis comprising a 40 s presputter to remove the gold coating over a rastered 15 μm × 15 μm area, centering of the secondary beam in the field aperture to correct for small variations in surface relief, and data acquisition in twelve four-second integration cycles. The magnetic field was locked at the beginning of the session using an NMR field sensor. Secondary ion signals (^{32}S and ^{34}S or ^{16}O and ^{18}O) were detected simultaneously using two Faraday detectors with a common mass resolution of 4860 (M/ΔM) for S and 2430 (M/ΔM) for O. Data were normalized for instrumental mass fractionation using a matrix-matched standard mounted with the sample mounts and analyzed after every sixth sample analysis. For barite, the S0327 reference material, with a conventionally determined $\delta^{34}S_{CDT}$ value of 22.3‰ and $\delta^{34}S_{CDT}$ value of 11.0‰ (values and standard courtesy of R.A. Stern, [51]; conventionally determined values have absolute uncertainties of ca. ±0.5‰ for both S and O due to interlaboratory differences). Determinations from our two sessions are shown in Tables 1 and 2 together with the sample analyses). Typical precision on a single $\delta^{34}S$ and $\delta^{18}O$ values, after propagating the within run and external uncertainties from the standard measurements was ±0.2‰ (1σ) and 0.23‰ (1σ) respectively. All results are reported with respect to the V-CDT [52] and V-SMOW for oxygen [53].

3. Results

3.1. Mineralogy

The mineralogy of the veins is dominated by barite and quartz with minor amounts of goethite, hematite, X-ray amorphous hollandite-group-like minerals, and MnO_2-like phases [38,54]. Additional K-feldspar and some galena were observed using SEM in the current study. Vein textures vary through the Cape Vani basement lavas and siliciclastic sediments vertical profile (Figure 1). Mineralogy and fluid inclusions are primarily studied on samples from the sediment-hosted veins. These veins are volumetrically dominated by coarse-bladed massive barite set in an amorphous silica and crystalline quartz matrix (Figure 3). Barite occurs as long rectangular crystals in various sizes and with random directions in the quartz matrix. At the barite–quartz interface, the barite is normally enclosed by a poorly crystalline silica phase. This silica phase is further out from the barite, successively transforming into crystallized vein-filling quartz (Figure 3), which contains numerous filamentous and spheroidal structures in a halo around the barite. These appear as fluid inclusions and have been classified based on their microbial-like appearance, as biomorphic type III inclusions (see below).
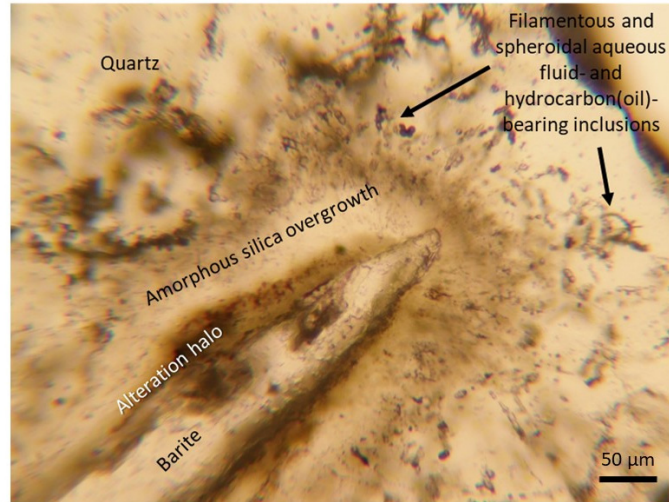
Figure 3. Microphotograph: An overview of the vein mineralogy. A longitudinal barite crystal overgrown in following order by a halo of hematite, a zone of amorphous silica, and the vein-filling quartz; the amorphous silica-quartz interface; and the quartz contain filamentous and spheroidal coexisting aqueous and oil-bearing type III inclusions (see text for descriptions and discussions).

3.2. Fluid Inclusion Petrography

Barite and quartz host primary fluid inclusions trapped during mineral growth (Figures 4–6). These were classified into three types on the basis of morphological and compositional criteria under transmitted and reflected light, fluorescent microscopy, Raman spectroscopy, and microthermometry: Aqueous (Type I), hydrocarbon- and hydrocarbon-bearing (Type II), and "Biomorphic" (Type III).

3.2.1. Type I

Type I are two-phase liquid-vapor (L-V) aqueous inclusions found in both quartz and barite. They are either liquid-rich (<25% vapor), vapor-rich (>70% vapor) (Figure 4A,B), or liquid-only (or L-rich with <10% unidentified vapor phase) inclusions; the latter may be isolated or paired, and in barite occasionally have funnel-like appearances characterized by parallel growth stages a few micrometers across (Figure 4C). Rarely, type I three- (or multiphase) phase [L-V ± solid(s)] fluid inclusions occur, which contain birefringent solid phases in addition to the vapor and liquid (see Figure 4D). The solid phase is equant to smoothly rounded, colorless and present only in a few inclusions. Type I inclusions are 5–30 μm in diameter and generally have smoothly rounded shapes with a few exceptions. Isolated aqueous L-rich and V-rich inclusions occur as well (Figure 4A,B).
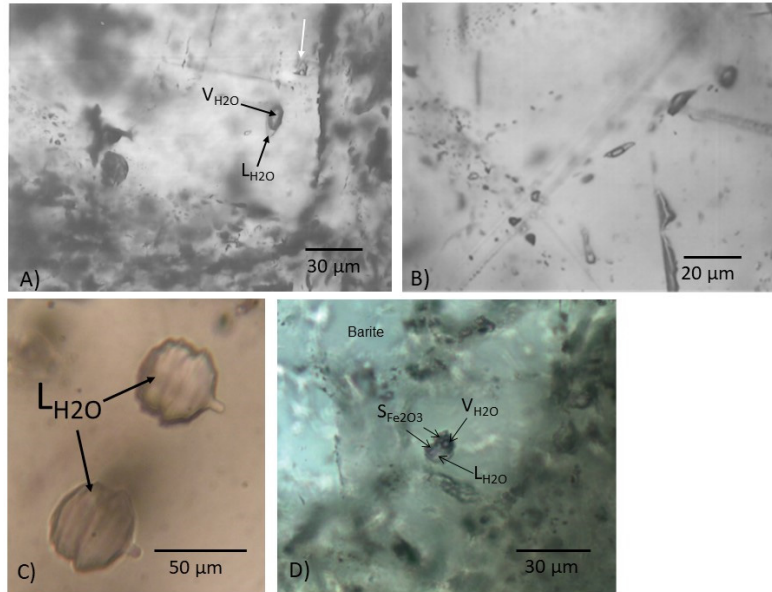
Figure 4. Transmitted light photomicrographs (Nichols) of type I aqueous fluid inclusions in quartz and barite. (**A**) Quartz (deep-water stratigraphy). Isolated pair of primary, type I inclusions, consisting of aqueous V-rich inclusion, with a thin sheath of liquid water (black arrow) coexisting with two-phase L-rich aqueous inclusion (white arrow). Indication of boiling conditions. (**B**) Barite (deep-water stratigraphy). Primary, two-phase V-rich type I aqueous inclusions. (**C**) Barite (shallow-water stratigraphy). Funnel-shaped, colorless one-phase liquid aqueous type 1 inclusions. Note parallel growth striations. (**D**) Barite (shallow-water stratigraphy). Liquid-rich type I multiphase [L-V ± solid(s)] aqueous inclusion with solid phases identified as hematite (Fe_2O_3) by Raman Spectroscopy.

3.2.2. Type II

Type II are hydrocarbon-bearing fluid inclusions that either occur as type III inclusions (see below) or in barite as (i) one-phase ($L_{hydrocarbon}$) inclusions (Figure 5A–C); (ii) two-phase ($L_{hydrocarbon}$-$V_{hydrocarbon}$) inclusions (Figure 5D,E); and (iii) three-phase (L_1-L_2-V) inclusions with liquid–vapor hydrocarbon ($L_{hydrocarbon}$-$V_{hydrocarbon}$) and a small amount of aqueous liquid (L_{H2O}), indicative of heterogeneous trapping (Figure 5F). The liquid hydrocarbon phase is mostly reddish-brown to reddish-orange, or pale yellow-orange to amber-colored, or colorless, under transmitted light (T). Hydrocarbon-bearing fluid inclusions range between 10 and 50 µm in size, have smooth appearance and, equant, spheroidal or irregular shapes (see type III below); again funnel-like appearance characterized by parallel growth stages occur in barite (Figure 5C).
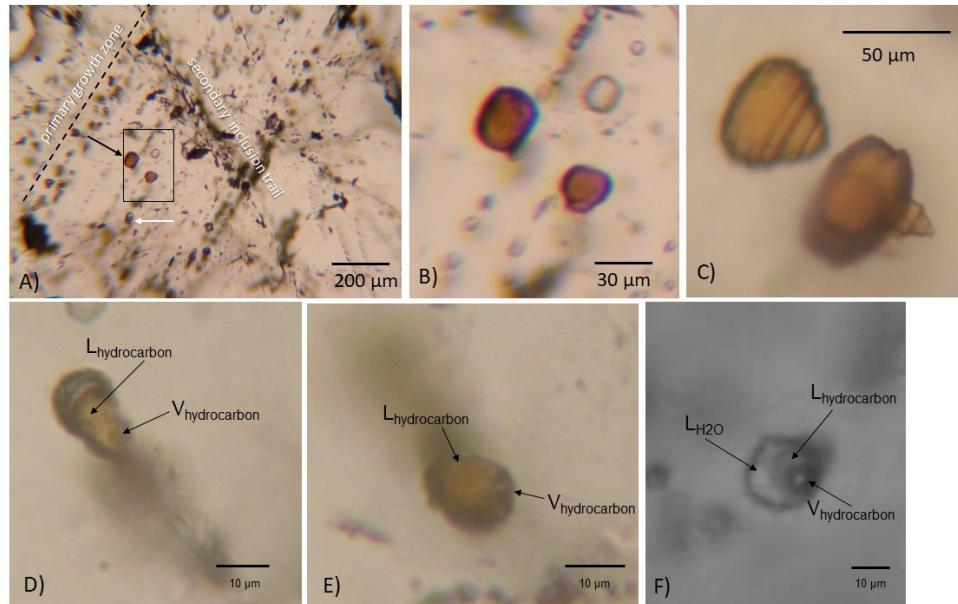
Figure 5. Photomicrographs in transmitted light of type II hydrocarbon-bearing (or oil-bearing) fluid inclusions in quartz and barite (shallow-water stratigraphy). (**A**) Barite. Inclusion-rich area showing coexistence of primary and pseudosecondary type I two-phase (L + V) aqueous inclusions (white arrow) with type II one-phase liquid-hydrocarbon (or liquid-oil) inclusions (black arrow), mainly concentrated in parallel planar arrays representing old growth surfaces; growth zones are obviously cut by secondary inclusions trails. (**B**) Details of panel (**A**). Smooth, equant-shaped, brownish-red-colored, type II single-phase liquid hydrocarbon inclusions. (**C**) Barite. Funnel-shaped, colorless one-phase liquid aqueous type I inclusions. Note parallel growth stages; (**D,E**) Turgid, slightly elongated, pale yellow-brownish, two-phase (L-V) oil-bearing inclusions; (**F**) Primary, isolated type II three-phase (L$_1$-L$_2$-V), aqueous liquid (L$_{H2O}$) + liquid hydrocarbon (L$_{hyc}$) + vapor hydrocarbon (V$_{hyc}$) hydrocarbon-bearing (or oil-bearing) fluid inclusion.

3.2.3. Type III

Type III inclusions are only found in samples from the main mine and were not recorded in veins hosted in rocks stratigraphically below the syngenetic mineralization. Type III inclusions represent type I and II inclusions that exhibit distinct biomorphic morphologies, such as filamentous, spheroidal, and rod-like structures and textures, and exceptional size range, and occur abundantly as a halo in the quartz around the barite (Figure 3). The filamentous inclusions are curvilinear, 10–20 μm in diameter and 20–200 μm in length (Figure 6A,C,D). They are segmented, and compartmentalized in either a repetitive fashion with the same distance between the partitions (Figure 6F,G) or in an irregular fashion with varying distance and size of the compartments (Figure 6A). They are sometimes turgid with bud-like outgrowths (Figure 6B). There are also twisted filamentous structures with diameters of a few micrometers (Figure 6H). The spheroidal microstructures are 10–30 μm in diameter and either circular or oval in shape (Figure 7). Some are bottle-shaped with a short tail-like filamentous outgrowth at one end, which results in a "spore-like" appearance (Figures 5D and 7A,B). The oval microstructures can be double, which results in a "peanut-like" appearance (Figure 7D–F). The spheroidal and filamentous inclusions are associated with each other and sometimes combined forming transitions between both types (Figures 5D,E, 6B, and 7A,D,E). Finally, filamentous type III fluid inclusions frequently contain an equant translucent brownish daughter solid phase that was identified as hydrocarbons by Raman spectroscopy (Figures 6E,É′ and 8).

In most samples, Type I aqueous vapor-rich (>90 vol.%) and liquid-rich inclusions coexist (Figure 4A,B). In addition, Type II hydrocarbon-bearing inclusions are found in barite and quartz,

whereas biomorphic Type III inclusions are only found in quartz from the samples collected within the mine (Figure 2A–C). Moreover, barite from within the mine also contains numerous primary and pseudosecondary one- or two-phase Type I and one-phase Type II fluid inclusions, with a size of up to 50 µm, that coexist concentrated in parallel planar arrays representing old growth surfaces, along successive crystal margins (Figure 5A,B), or occur disseminated within barite. Secondary inclusions can be differentiated from those inclusions trapped during mineral growth by their occurrence as inclusions trails that crosscut growth zones (Figure 5A).
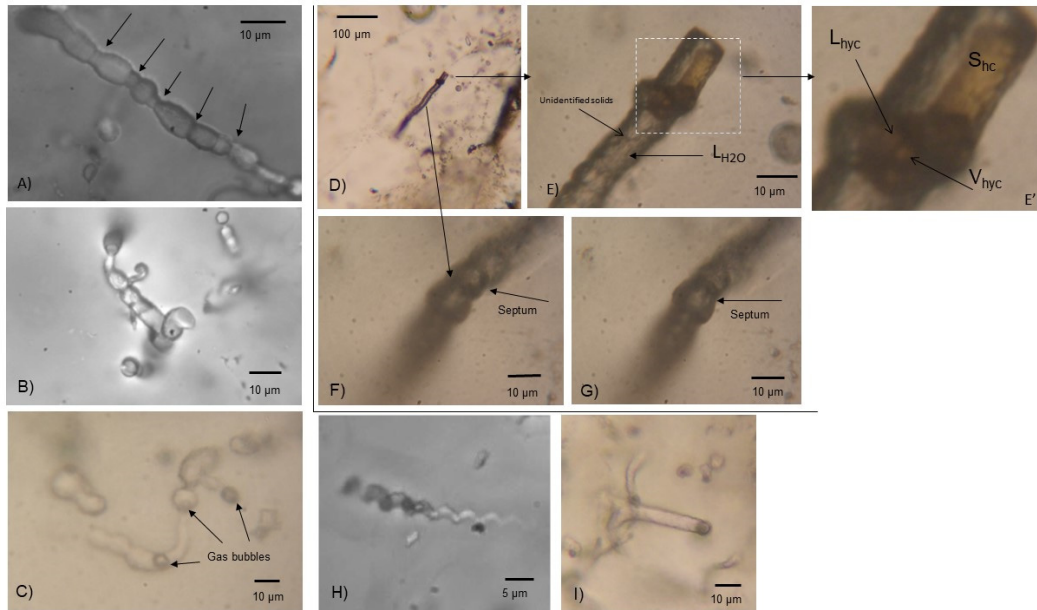

Figure 6. Transmitted light microphotographs of type III filamentous inclusions in quartz. (**A**) Large (~70 µm) isolated, primary, aqueous single-phase liquid (L) inclusion with septa (black arrows). (**B**) Filamentous, aqueous liquid (L_{H2O}) or liquid hydrocarbon (L_{hyc}) inclusions, with dark solid phase (bitumen) and no V phase. Note the knob-like outgrowths and/or associated spheroidal microstructures. (**C**) Filamentous and spheroidal aqueous or hydrocarbon (oil) two-phase (L + V) inclusions with transitions between both types including turgid appearance. (**D**–**G**) Large filamentous, multiphase, mixed aqueous (L_{H2O}) and hydrocarbon (L_{hyc}-V_{hyc}-S_{hyc} ± solids) inclusion. Note inclusion divided by septa, with an outgrowth at one end. (**H**) Small, twisted, filamentous aqueous multiphase (L-V-S) inclusions. (**I**) Filamentous, two-phase (L-V) aqueous or hydrocarbon inclusions.
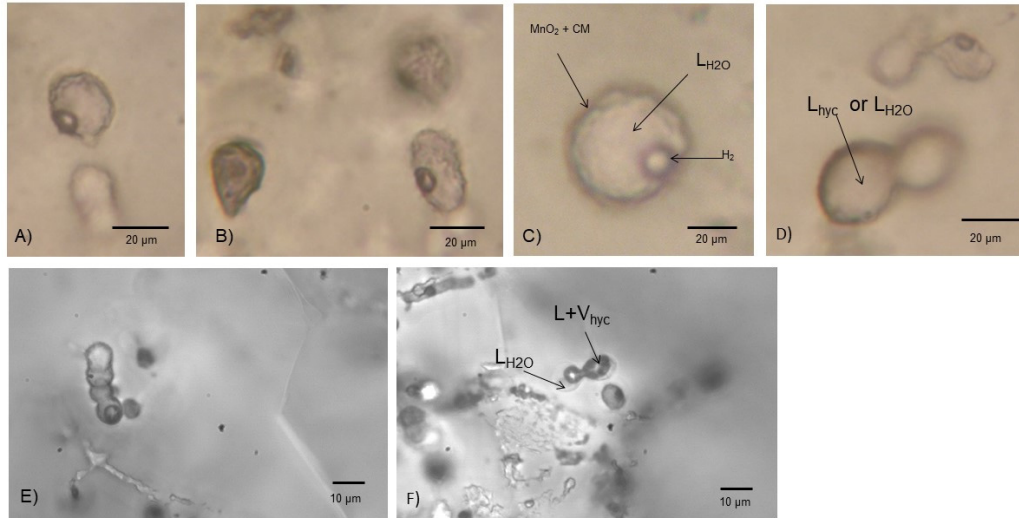
Figure 7. Transmitted light microphotographs of spheroidal aqueous and hydrocarbon-bearing type III fluid inclusions in quartz. (**A**) Spheroidal aqueous two-phase (L-V) inclusion with a "spore-like" shape and turgid appearance. (**B**) An oval aqueous two-phase (L-V) inclusion to the right and one "spore-like" leaked inclusion to the left. (**C**) Two phase aqueous inclusion with a H_2-gas phase. (**D–F**) "peanut-like" one-phase ($L_{hydrocarbon}$ or L_{H2O}) (**D**), two-phase ($L_{hydrocarbon} + V_{hydrocarbon}$ or $L_{H2O} + V_{H2O}$) (**F**), and mixed three-phase (L_{H2O}-L_{hyc}-V_{hyc}), hydrocarbon-(oil-)bearing type III inclusions, coexisting with aqueous type I L-V inclusions.
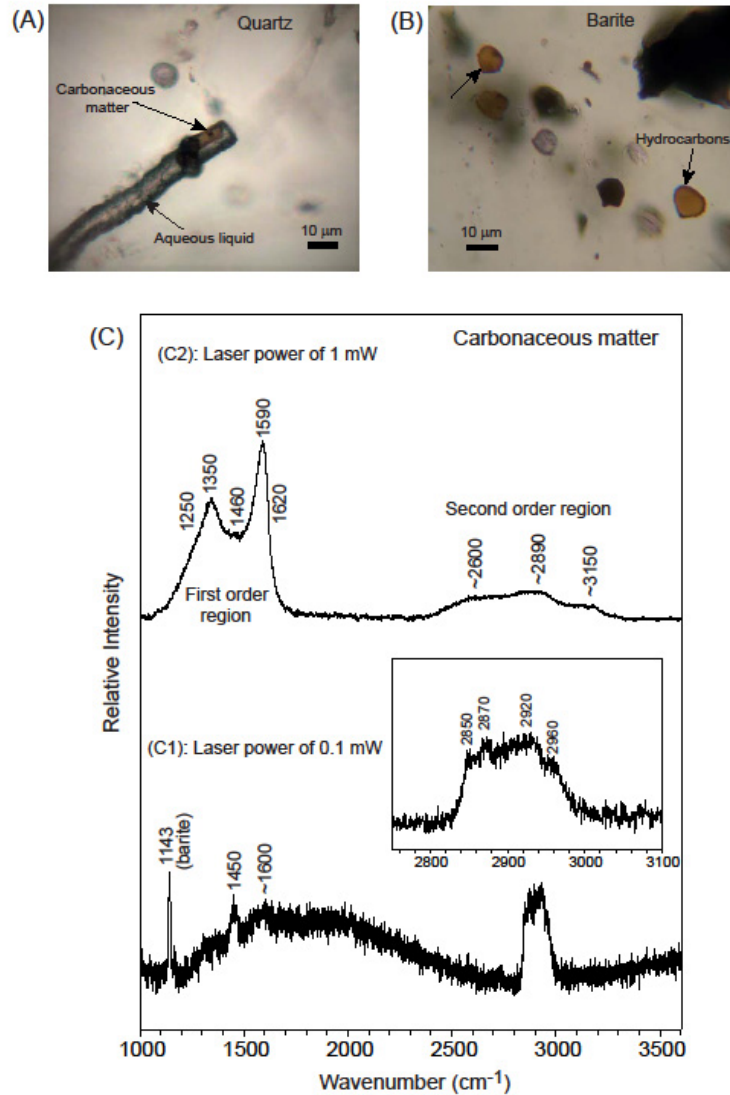
Figure 8. Raman spectrum of brownish phases captured in (photo **A**) a filamentous curvilinear multiphase, mixed aqueous (L_{H2O}) and hydrocarbon [L_{hyc}-V_{hyc}-S_{hyc} ± solid (s)] inclusion in quartz. The Raman spectrum is obtained at the tip of the upper arrow. Raman spectrum obtained in (photo **B**) funnel-like one-phase (L) hydrocarbon-bearing type II inclusions in barite, at the tip of the upper arrow. The graph in (**C**) shows Raman spectra in the 1000 to 3600 cm^{-1} range. The inset shows a magnified part in the 2750–3100 cm^{-1} region. The spectra are similar for inclusions in both barite and quartz. The weak intensity of spectrum (**C1**), identified as hydrocarbons, was obtained using a low laser power of 0.1 mW, and spectrum (**C2**) shows that by increasing the laser power to 1 mW on the same inclusion, the result was a laser induced photodegradation of the structures with a transformation to a poorly ordered carbonaceous matter (solid).

3.3. Fluid Inclusion Analyses

3.3.1. Microthermometry

In total, microthermometric data were obtained from 143 fluid inclusions hosted in barite and quartz. Microthermometric data were collected for two-phase (L-V) aqueous Type I and Type II fluid inclusions hosted in barite and quartz as well as biomorphic Type III inclusions in quartz. The data are presented in Figure 9, and Table S1, and described below. First, ice melting temperatures (Tfm-ice) of inclusions, where observed, occur between −42 °C and −30 °C, and suggest the possible

presence of divalent cations such as magnesium. Additionally, the occurrence of hematite in colorless inclusions suggests presence of $FeCl_2$ in the barite-hosted fluid inclusions. Final ice melting temperatures (Tm-ice) range from −0.2 to −12.4 °C (median: −7.0 °C), which correspond to salinities between 0.3 and 16.3 wt.% NaCl eq. (median: 10.6 wt.% NaCl eq.) (Figure 9a) (calculated using the method in [55]). Homogenization temperatures (Th) vary from 95 to 297 °C (median: 148 °C) (Figure 9b). High temperatures (>200 °C) are exclusively recorded in barite and probably represent necked/leaked inclusions. Figure 10 shows how fluid inclusion homogenization temperatures (Th) and last ice melting (Tm-ice) co-vary with data discriminated by hosting mineral phase and location within the mine.
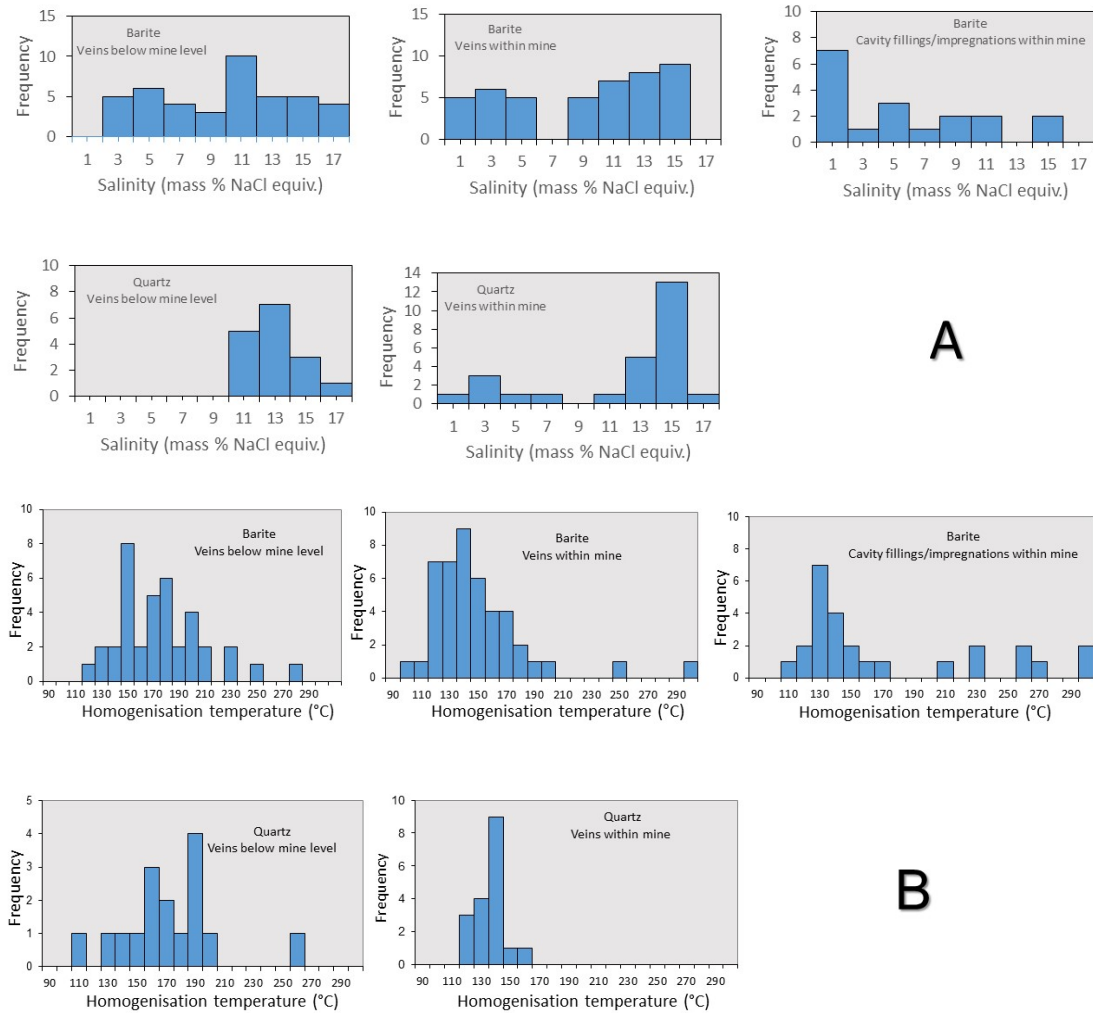

Figure 9. Histograms showing the distribution of (**A**) salinity and (**B**) homogenization temperatures for fluid inclusions discriminated by host mineral and sample stratigraphic level.
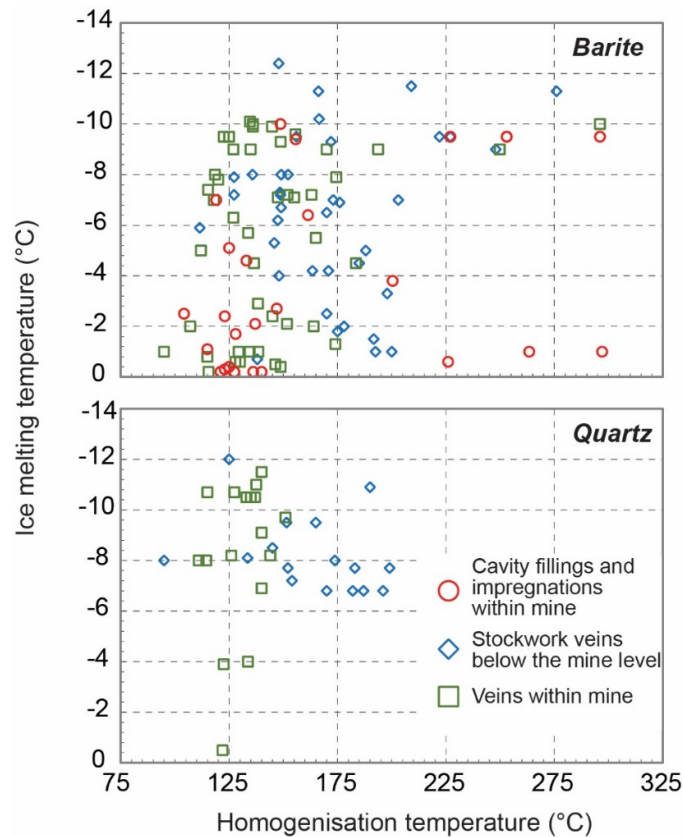
Figure 10. Scattergram of homogenization temperature versus salinity with individual points discriminated by host mineral (see text for details).

3.3.2. Raman Spectroscopy

Raman spectroscopy analysis was undertaken on

(i)　　　filamentous and spheroidal quartz-hosted Type III fluid inclusions that contain a translucent tabular dull-yellow phase (Figures 8A and 11) and

(ii)　　funnel-shaped Type II inclusions in barite, that are filled with a pale yellow-amber to yellow-brownish phase (Figure 8B).

Each fluid inclusion type gave similar hydrocarbon spectra (Figure 8), even though the hydrocarbon phase in Type III inclusions appears in optical microscopy to be solid and that in Type II a liquid. To avoid decomposition of the included material, a low laser power of 0.1 mW was initially utilized in acquiring the Raman spectrum, seen in C1 in Figure 8. The weak intensity of the spectrum using the low laser power made characterization of this spectrum difficult. The inset in Figure 8C shows a magnified part in the 2750 to 3100 cm^{-1} region where a complex group of bands appears: two main bands at approximately 2870 and 2920 cm^{-1} with shoulders at 2850 and 2960 cm^{-1} can be assigned to C–H stretching vibrations. The band at 1450 cm^{-1} is diagnostic of alkane CH_2 units, and the band around 1600 cm^{-1} can be assigned to ring stretching vibrations of aromatic hydrocarbons [56]. With a higher laser power of 1 mW some photodegradation of the hydrocarbons was induced with resulting transformation of the hydrocarbons, both in quartz and barite. This verifies that the inclusions have a pristine hydrocarbon composition that is easily altered by the Raman laser to a material with the resulting characteristic bands (C2 in Figure 8) typical of poorly ordered carbonaceous matter. That is a first-order region that consists of five overlapping bands: one ordered band at 1590 cm^{-1} together with defect bands at 1250, 1350, 1460, and 1620 cm^{-1} [57,58], and a second-order region with overtone scattering.

In addition to the trapped aqueous phase (s) in two-phase (L-V) Type III spheroidal inclusions in quartz (Figures 11 and 7C), the walls inside these structures, are encrusted with a Mn-compound

with bands at 505, 574, 625, and 645 cm^{-1} consistent with birnessite (Na, Ca)$_{0.5}$Mn$_2$O$_4$·1.5H$_2$O, [59]). The birnessite is associated with hydrocarbons (Figure 7A–C). Hydrocarbons were only detected in birnessite, not in the rest of these inclusions.

In these spheroidal two-phase L-V inclusions, Raman spectroscopy showed that the vapor phase consists of H$_2$ (Figure 11) with a strongest peak at 4155 cm^{-1} and with minor peaks at 4125, 4143, and 4160 cm^{-1} (reference spectrum in [60]). No other gases were found. H$_2$ was only detected in the spheroidal Type III inclusions.

Finally, solid phases, contained in some irregular aqueous (L-V) Type I fluid inclusions at the surface of barite crystals, were identified as hematite [61] (Figure 12).
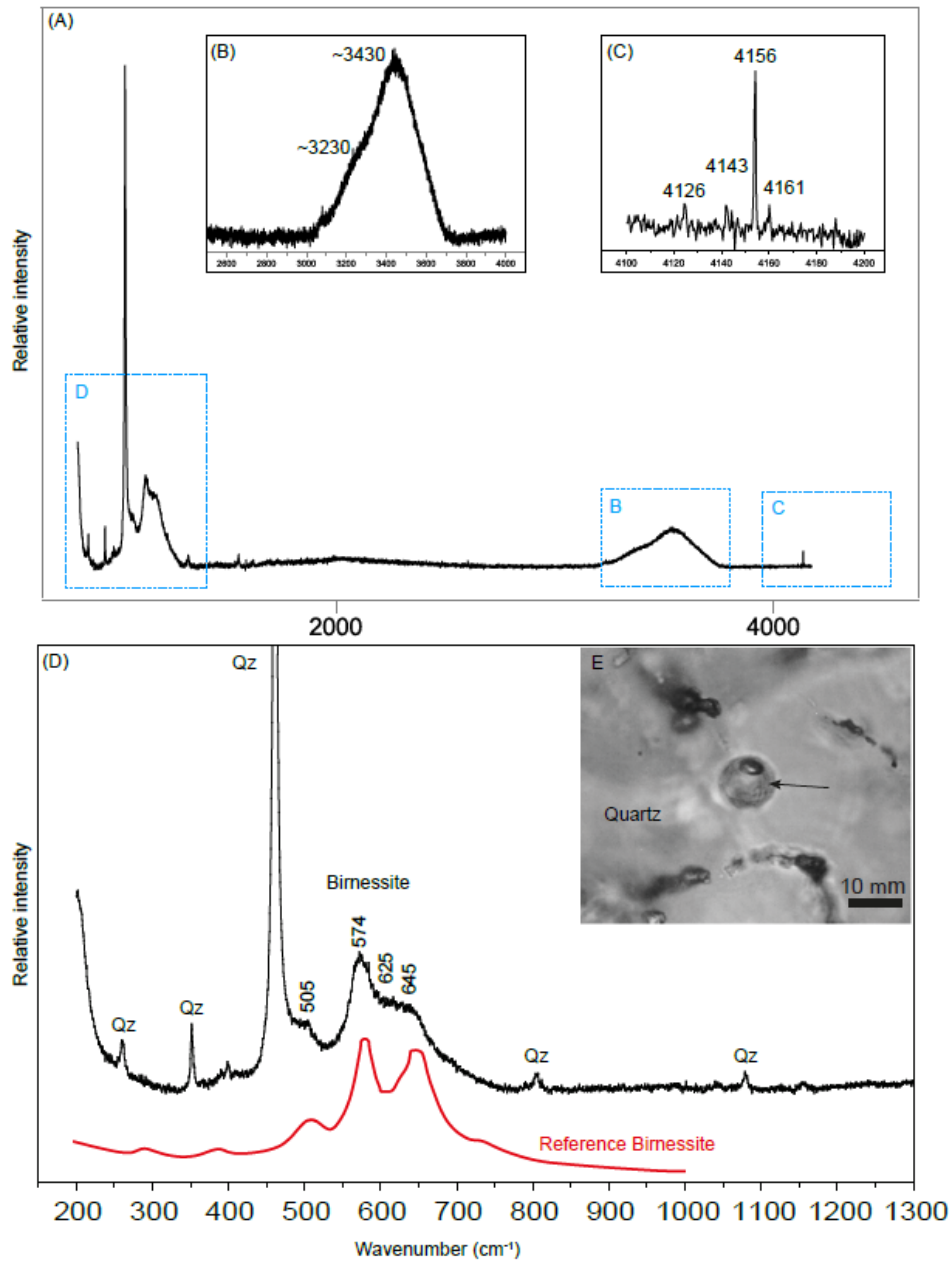

Figure 11. Raman spectrum of a "spore-like" spheroidal microstructure hosted by quartz. Graph (**A**) shows a Raman spectrum in the spectral range 150 to 4300 cm^{-1} of the microstructure. Graph (**B**) is a magnified spectrum of the wavenumber range 3000 to 4200 cm^{-1} (blue square B) and graph (**C**) of the range 4100 to 4300 cm^{-1} (blue square C), showing spectra of the vapor phase with a strongest peak at 4155 cm^{-1} and with minor peaks at 4125, 4143, and 4160 cm^{-1} indicative of H$_2$ [60]. Graph (**D**) is a

magnified spectrum of the wavenumber range 150–1300 cm^{-1}. The peaks designated as "Qz" in (**D**) is due to the quartz background. The Raman spectrum (**D**) with bands at 505, 574, 625, and 645 cm^{-1} of the outermost layer of the microstructure shown in the photo (**E**) are characteristic of a Mn-compound having a birnessite-like structure, reference spectrum (in red) of birnessite, $(Na, Ca)_{0.5}Mn_2O_4 \cdot 1.5H_2O$, from data in [59]. The broad bands of the 3100 to 3700 cm^{-1} region in (**B**) is attributed to O–H stretching vibrations, largely from liquid H_2O trapped within the spheroidal microstructure, with a possible minor overlapping contribution from the interlayer water of the birnessite structure.
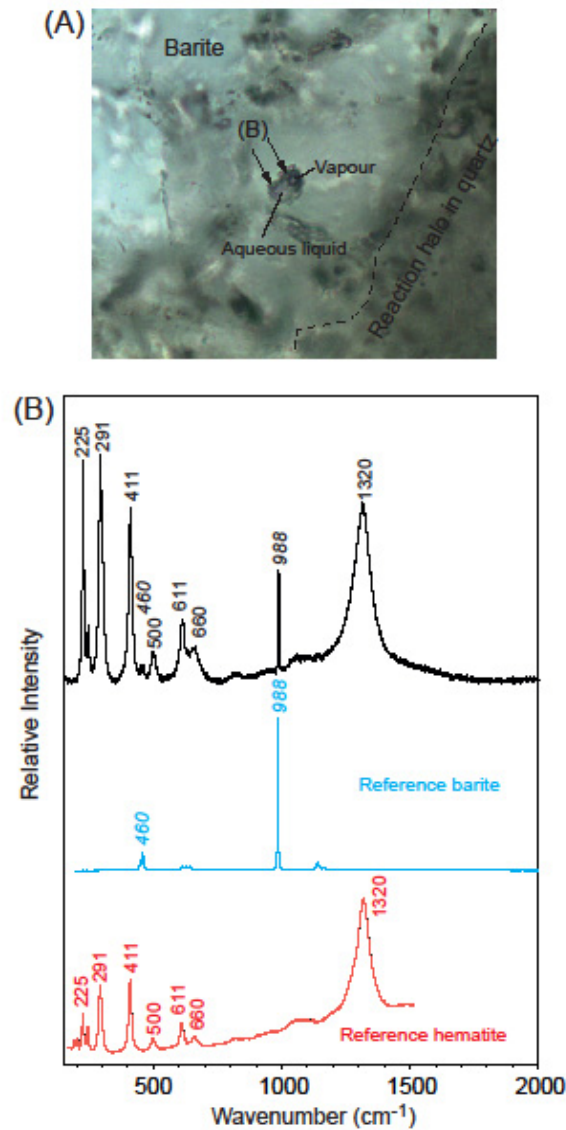

Figure 12. Raman spectrum measured of solid phases (arrows in photo **A**) in an aqueous two-phase liquid + vapor fluid inclusion from the outer part of a corroded barite crystal close to the turbid reaction halo in quartz that surrounds the barite (**A**). The indistinctive interface between barite and the blurred quartz zone is marked with a dashed line. Graph (**B**) shows the Raman spectrum in the 150 to 2000 cm^{-1} range of the phases identified as hematite, the wavenumbers for the peaks of the background barite is marked with italics. Reference spectra are from the RRUFF project database [61].

3.3.3. Staining with WGA-FITC and Fluorescence Microscopy

Using the Raman laser beam, a few of the larger hydrocarbon Type III inclusions were punctured and partly exposed. Most fluids were released when punctured, but some content on the walls

remained in the inclusion. The exposed inclusions were stained with WGA-FITC, which was introduced into the hollow inclusions and observed under fluorescence microscopy, where it was seen to bind to content remaining in some of these exposed inclusions (Figure 13). The binding of WGA-FITC was mostly localized to limited parts of the walls of the inclusions, not the entire interior.

3.4. Stable Isotopes

3.4.1. Carbon Isotopes

The $\delta^{13}C$ data obtained on bulk samples of the barite-quartz interface are given in Table 1. The range of $\delta^{13}C$ of the hydrocarbons was between −26‰ and −30‰ vs. PDB (Pee Dee Belemnite). This suggests that the principal carbon source is organic matter [62].

Table 1. $\delta^{13}C$ data obtained on bulk samples of the barite-quartz interface.

Sample	$\Delta^{13}C$ TOT vs PDB (‰)	%C
VA0518	−26.69	0.13
VA0520	−30.24	0.52
VA0522	−27.79	0.25
MI0344	−28.25	1.05

3.4.2. Sulfur and Oxygen Isotopes in Barite

The $\delta^{18}O$ and $\delta^{34}S$ barite bulk sample data are given in Table 2 and SIMS data in Tables S2 and S3. The oxygen ($\delta^{18}O$) and sulfur ($\delta^{34}S$) isotopic composition of Cape Vani barites range from +9.7‰ to +14.7‰ and +21.4‰ to +23.5‰, respectively, in bulk, and from +5.6‰ to +11.4‰ and +19.8‰ to +24.2‰, respectively, in the microscale determinations. Figure 14 shows the distribution of barite stable isotope date in $\delta^{18}O$-$\delta^{34}S$ space and spatiotemporal variation within a crystal.

Table 2. $\delta^{34}S$ and $\delta^{18}O$ stable isotope data for barite.

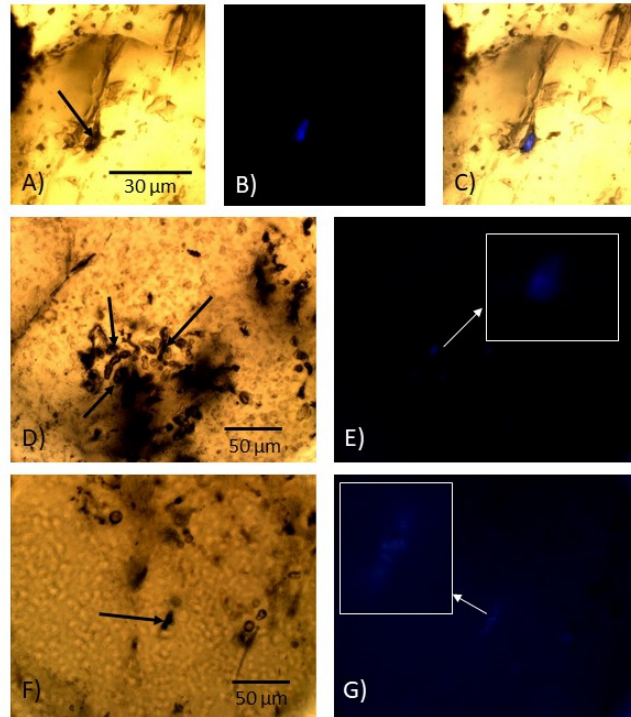| Sample	$\delta^{18}O_{V-SMOW}$ (‰)	$\delta^{34}S_{CDT}$ (‰)
MI-45B	11.2	23.2
MI-04-29	10.7	22.7
VA-19	10.5	23.5
VA-21	14.3	22.2
VA-01	14.7	21.9
SMO-bar	9.7	21.4
MI-52	10.5	24.3
VA-26	12.3	21.3
VA-05-02	11.4	22.6
VA-18	10.4	22.8

Figure 13. Microphotographs of cracked hydrocarbon-bearing type III inclusions before and after staining by WGA-FITC shown as series. (**A–C**) The same feature, (**D,E**) the same feature, and (**F,G**) the same feature. (**A**) Before staining, (**B**) after staining and under fluorescence light showing binding of WGA-FITC, and (**C**) mix of (**A**) and (**B**) to show localization of fluorescence to the structure. (**D**) Before staining, (**E**) after staining, (**F**) before staining, and (**G**) after staining. Black arrows mark the inclusions exposed by cracking and staining. Insets (**E,G**) are magnified images of the fluorescent parts of insets (**D,F**), respectively. The scale bar is the same for (**A–C**).
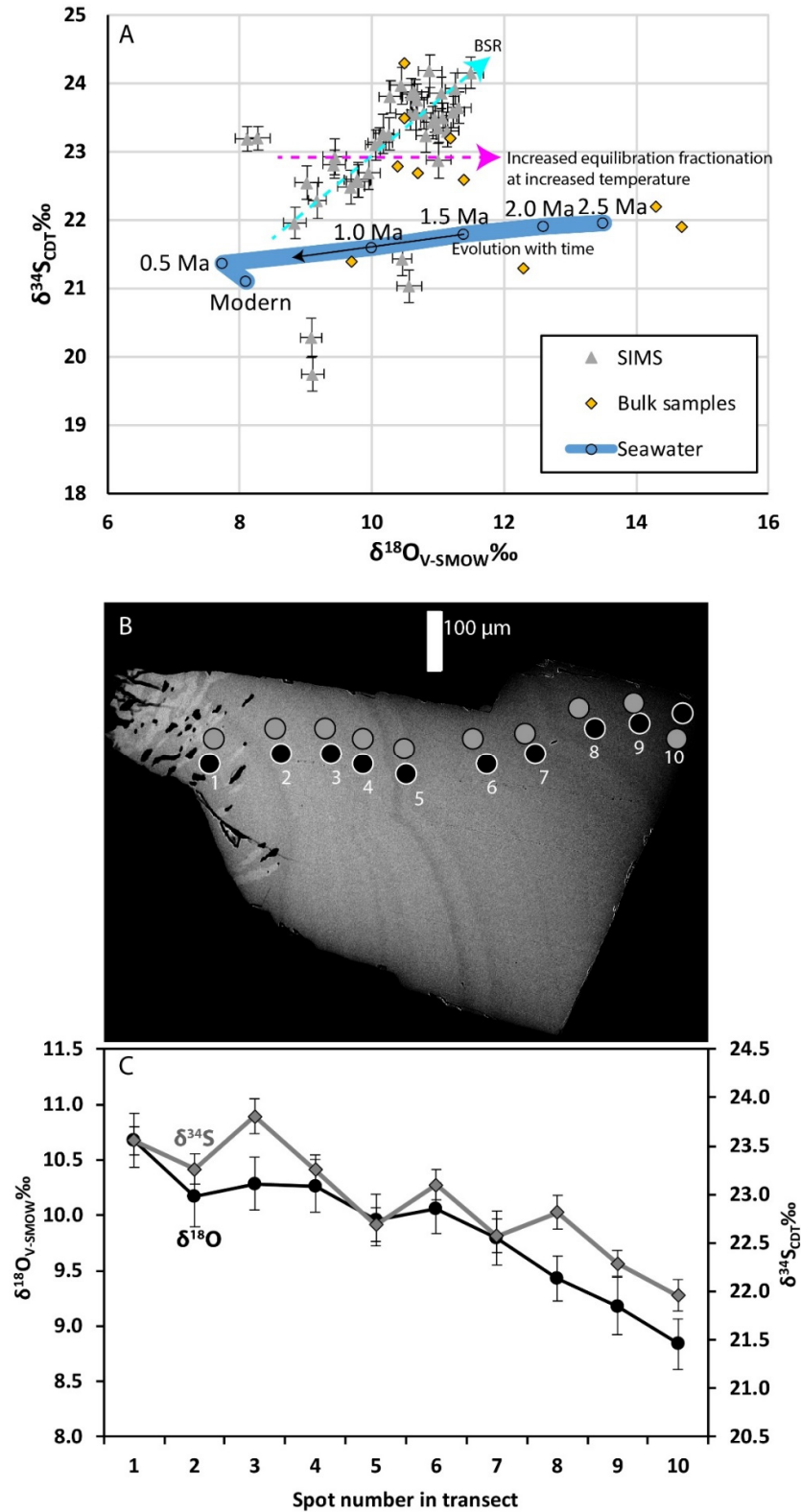
Figure 14. $\delta^{18}O$ and $\delta^{34}S$ values in barite. (**A**) $\delta^{18}O$ versus $\delta^{34}S$ for Vani barites (bulk and secondary ion mass spectrometry (SIMS) micro-analyses) with the variation seawater sulfate for the last 2.5 Ma overlain (circles connected by blue line, interpolated from [62–66], with trend with time indicated by black arrow). Also shown, is a schematic model showing isotopic trends for equilibrium fractionations between SO_4-H_2O (stippled magenta arrow), accelerated by high temperatures (temperature > 50 °C),

kinetic fractionations caused by variable sulfate reduction rates (stippled cyan arrow, modified from [67]). (**B**) SEM image of barite with growth zonation (growth from left to right) with SIMS spots for O (black) and S (grey) isotope analyses indicated. (**C**) Transect of isotopic values from B.

4. Discussion

The emphasis of this paper is to understand the unusual nature of the biomorphic Type III inclusions and the conditions at which they were trapped. A possible biological origin will be evaluated and discussed, but prior to this the environmental setting in which the proposed microorganisms existed will be described. The mineral succession in the studied system shows that the barite predates the quartz and that the putative microorganisms existed in the vein conduits, or in close proximity, during barite precipitation prior to quartz formation.

4.1. The Paleoenvironment of the Hydrothermal System

4.1.1. Interpretation of the Fluid Inclusion Data

Figure 9 shows how fluid inclusion homogenization temperatures (T_h) and last ice melting ($T_{m\text{-}ice}$) co-vary with data discriminated by hosting mineral phase and location within the mine. From this, a number of observations can be made:

(i) Homogenization data in barite show significant scatter towards high temperatures, most likely due to some post trapping modification and leakage during heating measurements. Notwithstanding this, there is a general trend of high (−1 °C) to low (−10 °C) $T_{m\text{-}ice}$ at relatively constant T_h (125–150 °C). This is much clearer in the quartz-hosted fluid inclusions from the mine samples.

(ii) Comparing mine and stockwork fluid inclusion data samples, in spite of the scatter of the barite data it would seem that fluid inclusions in the stockwork samples have higher T_h (25–50 °C) than fluid inclusions in samples from the mine.

(iii) The trend of increasing salinity at relatively constant or falling T_h is analogous to that recorded in the nearby Profitis Ilias and Chondro Vouno Au-Ag deposits, where it is interpreted to be the result of extensive open system boiling [34,68] and the Triades Pb-Zn-(Ag) deposit [36]. In these deposits, the highest homogenization temperatures and lowest salinities were interpreted to represent the composition of the hydrothermal fluid at initial boiling with the higher salinity lower T_h inclusions characterizing the boiled residual fluid.

(iv) Though most of the data exhibit salinities in excess of seawater ($T_{m\text{-}ice}$ < −2.1 °C), some inclusions exhibit $T_{m\text{-}ice}$ above −1.0 °C (1.5 wt.% NaCl eq.). This is somewhat like the low salinity–high T_h inclusions recorded at Profitis Ilias [68]. At Profitis Ilias, this was interpreted to result for the trapping of condensed vapor, and a similar origin is thought to be responsible for these fluid inclusions at Cape Vani.

4.1.2. Pressure–Temperature Considerations

Comparing the distribution of T_h–salinity data at Vani with the Profitis Ilias and Chondro Vouno Au-Ag deposits [34,68], we suggest it is rational to conclude, by analogy, that, at Vani, the processes of open system boiling also occurred, though at lower temperatures. Thus, as boiling is a key part of mineralization process fluid inclusion T_h is the temperature of the mineralizing hydrothermal fluid and accordingly the vapor pressure at homogenization is the trapping pressure. Taking fluid inclusions with salinities of 3.5 wt.% NaCl equiv. that homogenize at 125 °C to be representative of the hydrothermal fluid at initial boiling, we can estimate fluid densities and vapor pressures of 0.96 gcm^{-3} and 0.45 MPa (calculated using the method in [69]). This corresponds to a hydrostatic head of 47 m. This indicates an estimation of the maximum water depth during exhalative mineralization at Vani at ~50 m, which is in line with the observed microbial mat-related sedimentary structures [41], and the fluctuating water depths and tectonic uplift of ~250 m over the last 0.8 Myr [70].

Liquid hydrocarbons may have a hydrothermal origin analogous to modern-day hydrothermal hydrocarbons venting on the seafloor (e.g., Guaymas basin) [71–76]. However, liquid petroleum that is a typical product of sedimentary degraded organic matter has not been detected in modern-day hydrothermal shallow-water seafloor venting off the coast of Milos [77].

4.1.3. Interpretation of the S and O Isotopes in Barite

An δ^{34}S range of barite between +21 and +24‰V-CDT indicates a typical seawater source for the S [63], in accordance with previous interpretations of the epithermal mineralization system at Milos [34,37]. This suggests that barite formed from the mixing of hydrothermally derived Ba^{2+} and seawater SO_4^{2-}. However, as the Mn-Ba-Fe mineralization is young (<2.66 ± 0.07 Ma) [44], a more detailed interpretation can be made as the δ^{34}S and δ^{18}O stable isotope composition of seawater sulfate over the last 10 Ma is well constrained [63–66].

In addition to the bulk barite δ^{34}S and δ^{18}O values, which define a seawater signature, the SIMS isotope data of barite crystals in close relation to the biomorphic Type III inclusions show (with scatter) two main trends. First, on a crystal scale, transects show decreasing δ^{34}S and δ^{18}O values from core to rim of the zoned crystals in the veins (Figure 14B,C), and second a similar trend of positive correlation occurs between δ^{34}S and δ^{18}O values in the whole SIMS data set. This generally makes barite isotopically heavier in δ^{34}S than the contemporaneous seawater (Figure 14). The increase in δ^{34}S and positively correlated increase in δ^{18}O values are typically explained by barite formation from seawater sulfate that has been isotopically modified by variable degrees of bacterial sulfate reduction (BSR), such as observations at cold seeps [78]. However, the high Th (125 °C) of the barite fluid inclusions inhibits BSR as an in situ explanation for the isotope values; therefore, if BSR is the reason for the increase in ^{34}S and ^{18}O of the barite, the process must have occurred in lower temperature regimes of the seawater pool nearby. Partial or full re-equilibration of sulfate δ^{18}O with water δ^{18}O, which can occur when temperatures are 50 °C or above [79], may have occurred in the hydrothermal environment of Cape Vani as an additional mechanism for the re-equilibration of δ^{18}O in barite via interaction with heated seawater and geothermal fluids to heavier values. In addition, the fact that rims of the barites are isotopically lighter in terms of O can be explained by lower degrees of re-equilibration over the course of the hydrothermal pulse and falling temperatures (Figure 14). This scenario is in line with a drop in temperatures required to allow microorganisms to colonize the outermost barite crystal facies (see discussion of biomorphic Type III inclusions below). Seawater has over the last 2.5 Ma systematically decreased in δ^{18}O, from +13.5 to 8.0‰ [63–66]. Consequently, the drop in δ^{18}O during the cycle of barite precipitation could reflect decreasing δ^{18}O of the contemporaneous seawater sulfate. Such a correlation implies that the major population of barite targeted by micro-analysis, started to precipitate at ~1.5 Ma (Figure 14A) and continued for 1 Ma or more. Hydrothermal systems generally have lifetimes < 0.1 Ma [80]. As a result, the timespan, implied by the Vani barite δ^{18}O data is an order of magnitude longer than generally accepted for the life span of a hydrothermal system. Furthermore, if the barite δ^{18}O data were the result of precipitation from unmodified contemporaneous seawater, the combine δ^{34}S-δ^{18}O data would be expected to more closely follow the seawater evolution curve. Thus, though it is clear Cape Vani barites do not exhibit the extreme enrichments recorded in some cold seeps and open system conditions are most likely, the barite δ^{34}S and δ^{18}O data are best interpreted as being derived from seawater sulfate that has undergone some modification through BSR (not in situ because of high Th).

The hydrothermal environment responsible for preservation of the biomorphic Type III inclusions, formed with fluids cooling to <100 °C near the paleo-seafloor, in response to boiling, mixing with seawater, or conductive heat loss. Small quantities of the hydrothermal mineralizing fluid were captured as fluid inclusions in barite and in the filamentous and spheroidal microstructures in the quartz. Our interpretation is that barite and quartz formed in boiling hydrothermal water around 125 °C and at a shallow water depth (<50 m). In the present study, the high salinity of the fluid inclusions in barite is believed to represent the residual liquid phase of boiling seawater and implies that during barite precipitation the water gradually evolved from seawater salinity to an elevated salinity of 16 wt.% (NaCl).

The δ¹³C values of the hydrocarbons indicate that the principal carbon source is organic matter [62], and the most likely source of such hydrocarbons in a hydrothermal system is decomposed biomass from microbial communities. As the barite surfaces were the only solid substrates, except for the vein walls in the active hydrothermal system, it is probable they acted as substrate for microbial colonization. With time, increasing temperature in a second phase and mineral growth lead to the decomposition and slight boiling of these microbial communities and subsequent encapsulation by the growing barite.

4.2. Microbial Casts

The shape and morphologies of the Type III inclusions in quartz are far from typical for fluid inclusions in quartz, or any mineral [81], but correspond well to microbial morphologies [82]. The preservation as fluid inclusions suggest that the silica deposited as an amorphous accumulation in which the microorganisms were entombed and subsequently decomposed leaving fluid-filled cavities with preserved shapes of the original microorganisms on the inner walls. Some of the organic matter remained entrapped and is still present in the microstructures as hydrocarbons. The formation of the quartz and entombment of the microorganisms was probably an instant event at temperatures close to 100 °C, explaining the well-preserved cell walls with differing degrees of boiled cell interior. Thus, the fluid inclusions are putative casts of the original microorganisms rather than preserved organisms. With time, the amorphous silica transformed into the fine-grained crystalline quartz with the microorganisms preserved as fluid inclusions.

Since the structures are preserved as hollow casts, internal morphologies are missing. However, the external morphologies of the filamentous microstructures including curvilinear appearance, partitioning into separate cell-like compartments and branching are characteristic microbial filamentous morphologies and in favor of a biological interpretation of the structures [82]. The spheroidal structures with their range of perfect circular-, ellipsoidal-, and peanut-shaped features show characteristic morphologies for microorganisms. The size, however, exclude most prokaryotes except giant sulfur bacteria (GSB) that can range in size from 10 to 750 μm in diameter, and large cyanobacteria that tend to occupy spheroidal sheaths, ~60 μm in diameter. Cyanobacteria, as well as algae, which also correspond in size to the current microfossils are dependent on photosynthesis and occur exclusively in the photic zone with a few exceptions [83]. Owing to the occurrence of the presumed microorganisms at depth in narrow fractures, photobionts are not considered further as a possibility in the interpretation of the biological affinity of the microbial casts.

The filamentous structures with disc-shaped or cylindrical cells arranged as trichomes correspond in size and morphology to filamentous GSB belonging to Beggiatoaceae [84], but they also correspond to fungal hyphae, characterized by repeated septations [12]. The ellipsoidal and near circular inclusions are larger than most prokaryotic cells except GSB, but they correspond in size to fungal yeast cells as well [12,85]. GSB occur as both filamentous and non-filamentous morphotypes [84,85]. The latter is characterized by a large central vacuole that is filled with a noncytoplasmic fluid. At death, the microbes leave behind an empty core that can occupy >90% of the cell biovolume. Sulfur compounds could not be recognized in the Milos structures. However, the cytoplasmic sulfur vesicles of GSB disappear at death of the microorganisms with loss of the large central vacuole, thus sulfur is not to be expected in dead or fossilized GSB [86].

The size and morphology of the spheroidal inclusions characterized by bottle-, oval-, or ellipsoid- shaped, or near-circular structures with short tail-like filamentous outgrowths, correspond to spore-like morphologies. The transitions between filaments and near-circular structures suggest that they might represent sporophores or conidiophores forming at the tip of bacterial filaments or fungal hyphae [12]. Prokaryotic spores never exceed a diameter of 2–3 μm [82,87], thus spore-forming prokaryotes are excluded for further interpretation. GSB are not spore-forming, and are thus also excluded as an option [82]. This leaves fungi as the most likely option in respect to morphology [12]. In fact, fungal spore formation is similar to bud-like outgrowths, which is observed in our samples [12].

The successful staining with WGA-FITC of the inclusion interiors, provide biochemical support for a biogenic interpretation of the biomorphic inclusions. WGA-FITC binds to N-acetylglucosamine, which is a biopolymer in cell walls of many organisms. The presence of N-acetylglucosamine in the biomorphic inclusions is in agreement with a biological origin of the inclusions, but also shows that the organic content is indigenous to the inclusions and does not represent trapped hydrocarbons from the hydrothermal fluids. The staining with WGA-FITC and detection of N-acetylglucosamine is also in support of a fungal interpretation. WGA-FITC has an especially high affinity to chitin, a component in fungal cell walls, not present in bacteria and archaea. WGA-FITC is widely used for selective staining, for example, to differentiate between fungal hyphae and filamentous prokaryotes in soil samples or to distinguish fungal hyphae in mycorrhizae [46,88]. Gram-negative bacteria have N-acetylglucosamine in their inner cell walls, whereas Gram-positive bacteria have it in their entire cell walls, but in low amounts. WGA-FITC was shown to bind to a few Gram-positive bacteria by Fife et al. [89]; however, Montgomery et al. [90] showed that WGA-FITC binds to neither Gram-negative nor Gram-positive bacteria and concluded that the amounts of N-acetylglucosamine in bacteria are too limited to be stained. Besides, the bacterial options for the current fossils including GSB and cyanobacteria are exclusively Gram-negative [82,85,91]. WGA-FITC has been used to detect chitin in marine sediments [90] and for studying the fungal decomposition of organic matter in aquatic sediments [92]. WGA-FITC was used to detect chitin in fossilized fungal hyphae preserved in carbonate veins in subseafloor basalts collected at Koko Seamount, Pacific Ocean [10]; thus, its usage for chitin staining in fossil fungi in geological samples has been documented in previous studies. It is highly likely that the staining of WGA-FITC represents detection of chitin in the microbial casts, which rules out the possibility that the structures represent fossilized prokaryotes. Based on (1) geological context, (2) size and morphology corresponding to fungi, and (3) staining of WGA-FITC in favor of chitin detection we propose the biomorphic type III inclusions to represent remnants of fungi. The filamentous inclusions are interpreted as casts of fungal hyphae, and the spheroidal inclusions as fungal spores.

Despite being largely neglected in geomicrobiological investigations, fungi have been shown to be abundant and highly diversified in hydrothermal systems, methane seeps and marine sediments [5,93,94]. Fossilized fungi have been reported from subseafloor basalts indicating a deep and frequent presence in the ocean floors [7,8].

The large number of hydrocarbon inclusions at the barite growth zones indicates an abundance of organic matter at the barite–quartz interface, which probably represents degraded microbial communities that colonized the barite surfaces. Assuming the $\delta^{13}C$ values of bulk C represent the hydrocarbon content of the fluid inclusions, they are in support of a biological origin of the hydrocarbons. Thus, the barite surfaces at the time of fungal colonization were rich in organic matter easily accessible for the heterotrophic fungi. The temperature of the system could have been, according to the homogenization temperatures from the fluid inclusions, ~100 °C. This is well above the known temperature limit for thermophilic fungi that have a maximum temperature of growth of 62 °C [95]. However, the measured temperatures probably do not represent the mean temperature regime that prevailed in the system, but merely fluids with temporarily elevated temperatures due to extreme boiling and vaporization (fluid inclusion and amorphous silica evidence). The boiling of the microorganisms clearly shows that they could not tolerate temperatures around 100 °C and that the temperatures were lower in between the mineral forming events. Fluid inclusion measurements made on secondary carbonates in veins hosted in subseafloor basalt in which microorganisms were entrapped and subsequently fossilized show a similar trend [96]. The fluids that formed the vein-filling carbonates ranged in temperatures from 100 to 250 °C, whereas the microorganisms that colonized the fracture system prior to the mineral formation must have lived at temperatures below 100 °C, indicating that the mineral-forming fluids were introduced as pulses in the system [96].

4.3. Mn-Coating of Spheriodal Type III Inclusions

The aqueous spheroidal Type III fluid inclusions in quartz with morphologies similar to spores differ notably from the other types of inclusions in that they have Mn-oxide (birnessite, (Na,

$Ca)_{0.5}(Mn^{4+}, Mn^{3+})_2O_4 \cdot 1.5H_2O)$-coated walls and a H_2 gas phase. The ability of microorganisms to oxidize Mn(II) to Mn(III/IV) oxides is found throughout the bacterial and fungal domains of life [97]. The presence of abundant Mn-oxides in the feeder dykes and the related Vani Mn-ore [42] shows that there was an abundance of soluble Mn(II) in the system available for microorganisms to utilize. One of the major pathways in which microorganisms oxidize Mn(II) is via the reaction

$$Mn^{2+} + H_2O_2 = MnO_2 + 2H^+ \text{ [98]} \tag{1}$$
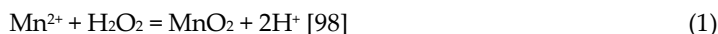
In this reaction, the microorganisms oxidize Mn(II) with peroxide (H_2O_2) using catalase as the enzyme that promotes the reaction. This is a common reaction pathway among Mn-oxidizing bacteria, and the major pathway among Mn-oxidizing fungi [99].

The presence of Mn-oxides at the inclusion walls is probably due to localized Mn-oxidation at what represents the former walls of the spores. The oxidation of Mn(II) by spores but not by vegetative cells is a phenomenon common among many spore formers [98]. A number of spore forming marine Bacillus are known to enzymatically oxidize soluble Mn(II) to Mn(IV) oxides [100]. In Bacillus, SG-1 Mn(II) are bound and oxidized by a protein in the exosporium, which results in the deposition of Mn-oxides at the spore surface [98]. Among isolated bacilli, Mn-oxidation was shown to be absent in vegetative cells but dependent on cells that were in the process of sporulating [98]. The diameters of bacterial spores involved in Mn-oxidation are only a few micrometers and not in the size range of the current spheroidal inclusions [82]. The diameters of fungal spores, on the other hand, fit the size range of the current spore-like inclusions. Enzymatic oxidation of Mn(II) to Mn(IV) has been observed in the spores of an Acremonium-like fungus belonging to the Ascomycetes [99]. The authors showed that Mn(II) is oxidized to Mn(IV) at the asexual reproductive structures owing to the production of extracellular superoxide during cell differentiation. The Mn-oxide phase birnessite and the reactive oxygen species superoxide and hydrogen peroxide were colocalized at the base of asexual reproductive structures. Biomineralization of fungal spores by Mn-oxides has also been shown in fossilized zygosporic fungi obtained from dredged samples at the Vesteris Seamount, Greenland Basin. The hyphal mycelium was fossilized by the Fe-oxide phase limonite, whereas the spores were mineralized by romanechite-like Mn-oxides [16].

The physiological reason for Mn(II) oxidation by bacteria and Ascomycetes fungi is unknown. The process has not been linked to energy conservation, and the rate or extent of growth by the organisms has not been enhanced in the presence of Mn(II) [101,102]. Superoxide formation by the Mn-oxidizing bacteria Roseobacter and the fungi Stilbella lineages, does not appear to be a response to available Mn(II). Cell differentiation is, for example, not enhanced in the presence of Mn(II), and thus the Mn(II) oxidation of these organisms is likely an unintentional side reaction [99].

4.4. H_2-Content of Spheriodal Type III Inclusions

Molecular hydrogen in fluid inclusions is rarely reported, either because it is extremely volatile, and thus seldom captured in fluid inclusions, or because of its tendency to diffuse out of the inclusions and therefore almost only be found in environments associated with radiolysis, as in uranium deposits [103] or in melt inclusions [104]. The exact cause for the trapping of H_2 in the current inclusions is not obvious, but there is a clear link between the presence of H_2 gas and Mn-oxide coating on the inclusion walls; thus, it is reasonable to assume that the Mn-oxides prevent the H_2 from diffusing out through the quartz. H_2 is a reactive gas that becomes oxidized in the presence of most metals with the rare exception of a few, including Mn(-oxides) [105,106]. Laboratory experiments related to fuel cell development have shown that in a system containing CO and H_2 Au-doped Mn-oxides is one of the best candidates in selectively oxidizing CO while at the same time being inactive for the oxidation of H_2 [106]. The organic content in the current inclusions are, according to the Raman measurements, associated with the Mn-oxides while the H_2 gas is left unreacted. The lack of CO_2 in the inclusions indicates that no oxidation of the organic material has occurred; however, a selective adsorption of the organic matter over H_2 is a likely scenario. Thus, the Mn-oxide coating would not only trap the H_2 gas from diffusing out of the inclusions but also leave the gas intact and not oxidizing it.

The lack of serpentinization in the area greatly reduces the possibilities of an abiotic source of H_2. None of the minerals in the paleohydrothermal system of Cape Vani can give rise to formation of H_2 abiotically, and radiolysis is not likely at these shallow water depths with the present mineralogy. Investigations at active vents on Milos give a disparate understanding indicating no [40] or slight (3.2% vol) flux of dissipating H_2 [77]. Methane, on the other hand, dissipates from the vents around Milos, but has been explained as mostly abiogenic (volcanic gas) in origin [107]. Most δD values of methane support an abiogenic source of hydrogen but some extremely low values (−377‰) indicate a different source [77,107,108]. These values are however explained as probably being "caused by unknown subsurface rock alteration processes" [107]. On the other hand, the hydrogen isotopic system is not very well understood in terms of abiotic and biological signatures. Heterotrophy seems to result in larger fractionation towards lower values compared to autotrophy, while the lower values coincide with abiotic fractionation [109]. In summary, the origin of H_2 in non-serpentinized hosted subsurface environments is seldom discussed in detail and it is difficult to deduce the origin geochemically [30].

The lack of external sources for H_2, the volatile nature of H_2, and the exclusive containment in Mn-oxide coated inclusions makes trapping of external H_2 highly unlikely. Also, the lack of trapped CO_2 and CH_4—two gases much more common in hydrothermal systems along the Hellenic Arc [40,77,107,108] and likely to be trapped in fluid inclusions—speaks against an external source for H_2. Instead, an internal source confined to the microbial structures is more likely. Organic matter and water are the two possible sources of H_2 in the inclusions. Absence of CO_2 in the inclusions rules out oxidation of organic matter, and splitting of water by manganese has, to our knowledge, not been reported previously. Thus, an abiotic internal formation of H_2 is unlikely. A biological origin of the H_2 would be a possible alternative considering the biological origin of the inclusions. In a microbiological context, the ability to produce H_2 is usually coupled to fermentation and has been observed in a relatively large number of microorganisms, usually linked to strict or facultative anaerobic metabolism among heterotrophs or photosynthesizers [30,110]. Biological production of H_2 is mediated by the enzyme hydrogenase, which catalyzes the reaction

$$2e + 2H^+ \rightarrow H_2 \text{ [111]} \tag{2}$$

This reaction reflects the ability of microorganisms to dispose "excess" electrons in the form of molecular hydrogen. This is common among prokaryotes like *Clostridium pasteurianum*, *Ralstona eutropha*, or *Desulfovibrio* spp [110], but also among diverse eukaryotes like ciliates, algae and fungi [112]. In eukaryotes, hydrogenases are critical to the function of the hydrogen-producing organelles hydrogenosomes [112]. In fungi, hydrogenosomes are only known from the obligate anaerobic gut fungi of the phylum Neocallimastigomycota [17,18]. Neocallimastigomycota are almost exclusively known from rumens of herbivores but have recently been found in environmental samples like the gut and coelomic fluid of the coastal sediment-dwelling sea urchin *Echinocardium cordatum* [113] and in the guts of the algae-grazing marine iguana *Amblyrhynchus cristatus* [114]. They have also been reported from landfill soils [115], as well as lacustrine [116], estuarine [117], and marine sediments [118]. This growing number of observations suggests that obligate anaerobic fungi not only exist as endosymbionts in rumens, but also in marine animals as well as free-living in anoxic sediments and soils. Hydrogen-producing anaerobic fungi have been hypothesized to play a similar ecological role in deep anoxic environments as they do in the guts where they provide H_2 to H_2-dependent prokaryotes like methanogens or acetogens [21]. Such anaerobic consortia is still to be observed in nature; however, fossilized communities of fungi and syngenetic pyrite with $\delta^{34}S$ signals indicative of sulfate reducing bacteria have been found in strict anoxic environments at 740 m depth in the Swedish crystalline basement, thus partly confirming such a deep anaerobic partnership [22]. The conditions in the current feeder veins of Milos is not supposed to be anoxic considering the presence of Fe- and Mn-oxides [42]; however, it is possible that the fluids were suboxic at times due to ingress of deeper anoxic hydrothermal fluids, and locally, in association with the barite surfaces due to microbial activity. The presence of galena in the barites as well as the abundant hydrocarbons associated with the barite and amorphous silica–quartz interface suggest anoxic conditions locally at

the barite surfaces. Besides, fungi are an underexplored group of microorganisms, especially in anoxic environments including deep settings, whose metabolism and resistance to oxygen depletion is far from investigated and understood [11]. A majority of fungi reported from the subsurface are fungi known as aerobes in surface environments. Their metabolisms in the anoxic subsurface environments are, however, unknown. Previously there was a clear distinction between aerobic and anaerobic eukaryotes; those who have mitochondria and those who have hydrogenosomes [119]. Aerobic and anaerobic eukaryotes were believed to be evolutionarily divided and anaerobic eukaryotes only to be found in the basal branches of the eukaryotic tree. However, studies have shown that hydrogenosomes are reduced mitochondria and that the reductive evolution of mitochondria to hydrogenosomes or other mitochondrial homologs is common across the eukaryotic tree [120]. The transition from mitochondria to hydrogenosomes is, in fact, a simple result of oxygen deficiency in the environment [121]. Thus, aerobic micro-eukaryotes exposed to permanent anoxia or suboxia certainly have the capability to adapt and develop anaerobic metabolic pathways over time. Besides, many facultative anaerobes possess hydrogenase and produce H_2 at suboxic conditions or conditions that oscillate between anoxia and suboxia. There is even aerobic H_2 production among certain bacteria, thus strictly anoxic conditions are not a requirement for H_2 production involving hydrogenase [110].

We suggest that the H_2 gas phase detected in the exceptionally preserved fungal spores from the paleohydrothermal system at Cape Vani, Milos, are the result of biologically produced H_2. The rapid entombment of the fungi captured the H_2 in the structures, and with a change in temperature and pressure dissolved H_2 becomes less soluble and forms gas bubbles within the fluid inclusion that in very rare occasions, may stay trapped because of impermeable surroundings [122].

4.5. Biological Production of H_2 in Hydrothermal Environments

The abundance of fungal remains at the barite–quartz interface in the shallow-water stratigraphy of the Vani mine does not necessarily mean that fungi dominated the microbial communities of the feeder veins. Due to significant differences in cell wall composition fungi are more easily preserved than prokaryotes in subseafloor environments [7]. Thus, the fungal dominance is likely due to a bias in the fossilization rather than being a true reflection of the community structure. For example, the presence of twisted filaments with diameters of a few micrometers (seen in Figure 6H) corresponds more to morphologies of Fe- or Mn-oxidizing prokaryotes than to filamentous fungi [82], and suggests the communities to be diverse and composed of both prokaryotes and eukaryotes. Our results, however, show that fungi were present in abundance at the barite/amorphous silica open pore space (today quartz) interface, and that they are linked to H_2 production. It is difficult to quantify the biological production of H_2, and therefore evaluate its geochemical influence on a larger scale. Hydrothermal vents associated with ultramafic rocks have higher yields of H_2 outgassing compared to systems hosted in other geological settings, like basalt-hosted environments [28]. Thus, in a global perspective abiotic production of H_2 is likely dominant over biological. However, all H_2 diffusing from hydrothermal vents do not necessarily have to be abiotic in nature. Discrepancy between abiotic and biological H_2 at hydrothermal vents has to our knowledge, never been reported.

The production of extracellular polymeric substances in fungal/prokaryotic biofilms would act as an active trap preventing immediate dispersion of H_2 from the micro-niche. Once released from the fungal cell the H_2 would be kept from immediate escape from the biofilm community, and thus available for prokaryotic metabolism. Abiotic H_2 production, on the other hand, is restricted to certain reduced minerals, and thus, first, is spatially unevenly distributed and, second, is not continuously produced; two factors that may be crucial for sustaining communities of H_2-dependent prokaryotes. Besides, the volatile nature of H_2 would disperse the H_2 into the system making it unavailable for prokaryotes to utilize metabolically. Biologically produced H_2 in a biofilm would be a continuous source that potentially could support a local community of H_2-dependent prokaryotes. Fungi, and other micro-eukaryotes equipped with hydrogenosomes as well as fermenting prokaryotes, may partly be responsible for the H_2 production in hydrothermal, deep environments, and locally play a significant role in supporting H_2-dependent prokaryotes.

5. Conclusions

Fluid inclusions with characteristic microbial morphologies hosted in quartz from feeder veins associated with the Vani Mn-ore deposit formed by mixing of deep hydrothermal fluids and seawater at the Greek island Milos were investigated. Based on morphological traits and the presence of chitin detected by the staining with WGA-FITC under fluorescence microscopy, the fluid inclusions were interpreted as fungal imprints. Spheroidal two-phase inclusions, interpreted as fungal spores, are unique by their coating of Mn-oxide birnessite and content of gas phase H_2. A fungal origin of the H_2 is inferred and we suggest micro-eukaryotes like fungi to be a, so far unrecognized, but significant source of H_2 in subsurface environments. Biologically produced H_2 can play an important role in supporting communities of H_2-dependent prokaryotes in both modern and ancient oceanic crust.

References

1.　Orcutt, B.N.; Sylvan, J.B.; Knab, N.J.; Edwards, K.J. Microbial ecology of the dark ocean above, at, and below the seafloor. *Microbiol. Mol. Biol. Rev.* **2011**, *75*, 361–422.

2.　Edgcomb, V.P.; Kysela, D.T.; Teske, A.; de vera Gomez, A.; Sogin, M.L. Benthic eukaryotic diversity in the Guaymas Basin hydrothermal vent environment. *Proc. Natl. Acad. Sci. USA* **2002**, *99*, 7658–7662.

3.　López-García, P.; Vereshchaka, A.; Moreira, D. Eukaryotic diversity associated with carbonates and fluid-seawater interface in Lost-City hydrothermal field. *Environ. Microbiol.* **2007**, *9*, 546–554.

4.　López-García, P.; Phillipe, H.; Gaill, F.; Moreira, D. Autochthonus eukaryotic diversity in hydrothermal sediment and experimental micro-colonizers at the Mid-Atlantic Ridge. *Proc. Natl. Acad. Sci. USA* **2003**, *100*, 697–702.

5.　Nagano, Y.; Nagahama, T. Fungal diversity in deep-sea extreme environments. *Fung. Ecol.* **2012**, *5*, 463–471.

6.　Hirayama, H.; Abe, M.; Miyazaki, J.; Sakai, S.; Nagano, Y.; Takai, K. Data Report: Cultivation of microorganisms from basaltic rock and sediment cores from the North Pond on the Western Flank of the Mid-Atlantic Ridge, IODP Expedition 336. *Proc. Int. Ocean Drill. Prog.* **2015**, *336*, doi:10.2204/iodp.proc.336.204.2015.

7.　Ivarsson, M.; Holm, N.G.; Neubeck, A. The deep biosphere of the subseafloor igneous crust. In *Trace Metal Biogeochemsitry and Ecology of Deep-Sea Hydrothermal Vent Systems*; Demina, L.L., Galkin, S.V., Eds.; Springer: Berlin, Germany, 2015; pp. 143–166.

8. Ivarsson, M.; Bengtson, S.; Drake, H.; Francis, W. Fungi in deep subsurface environments. In *Advances in Applied Microbiology*, Sariaslani, S., Gadd, G., Eds.; Academic Press: London, UK; Elsevier: London, UK, 2018; Volume 102, pp. 83–116.

9. Bengtson, S.; Rasmussen, B.; Ivarsson, M.; Muhling, J.; Broman, C.; Marone, F.; Stampanoni, M.; Bekker, A. Fungus-like mycelial fossils in 2.4 billion-year-old vesicular basalt. *Nat. Ecol. Evol*. **2017**, *1*, 0141.

10. Ivarsson, M.; Bengtson, S.; Belivanova, V.; Stampanoni, M.; Marone, F.; Tehler, A. Fossilized fungi in subseafloor Eocene basalts. *Geology* **2012**, *40*, 163–166.

11. Drake, H.; Ivarsson, M. The role of anaerobic fungi in fundamental biogeochemical cycles in the deep biosphere. *Fungal Biol. Rev.* **2018**, *32*, 20–25.

12. Webster, J.; Weber, R.W.S. *Introduction to Fungi*, 3rd ed.; Cambridge University: Cambridge, UK, 2007; p. 875.

13. Gadd, G. Geomycology: Biogeochemical transformations of rocks, minerals, metals and radionuclides by fungi, bioweathering and bioremediation. *Mycol. Res.* **2007**, *111*, 3–49.

14. Bengtson, S.; Ivarsson, M.; Astolfo, A.; Belivanova, V.; Broman, C.; Marone, F.; Stampanoni, M. Deep-biosphere consortium of fungi and prokaryotes in Eocene sub-seafloor basalts. *Geobiology* **2014**, *12*, 489–496.

15. Ivarsson, M.; Broman, C.; Gustafsson, H.; Holm, N.G. Biogenic Mn-oxides in subseafloor basalts. *PLoS ONE* **2015**, *10*, doi:10.1371/journal.pone.0128863.

16. Ivarsson, M.; Peckmann, J.; Tehler, A.; Broman, C.; Bach, W.; Behrens, K.; Reitner, J.; Böttcher, M.E.; Norbäck-Ivarsson, L. Zygomycetes in vesicular basanites from Vesteris Seamount, Greenland Basin—A new type of cryptoendolithic fungi. *PLoS ONE* **2015**, *10*, doi:10.1371/journal.pone.01333368.

17. Liggenstoffer, A.S.; Youssef, N.H.; Couger, M.B.; Elsahed, M.S. Phylogenetic diversity and community structure of anaerobic gut fungi (phylum Neocallimastigomycota) in ruminant and non-ruminant herbivores. *ISME J.* **2010**, *4*, 1225–1235.

18. Khejornsart, P.; Wanapat, M. Diversity of rumen anaerobic fungi and methanogenic archaea in swamp buffalo influenced by various diets. *J. Anim. Vet. Adv.* **2010**, *9*, 3062–3069.

19. Mountfort, D.O.; Asher, R.A.; Bauchop, T. Fermentation of cellulose to methane and carbon dioxide by a rumen anaerobic fungus in a triculture with *Methanobrevibacter* sp. Strain RA1 and *Methanosarcina barkeri*. *Appl. Environ. Microbiol.* **1982**, *44*, 128–134.

20. Hook, S.E.; Wright, A.-D.G.; McBride, B.W. Methanogens: Methane producers of the rumen and mitigation strategies. *Archaea* **2010**, *945785*, doi:10.1155/2010/945785.

21. Ivarsson, M.; Schnürer, A.; Bengtson, S.; Neubeck, A. Anaerobic fungi: A potential source of biological H_2 in the oceanic crust. *Front. Microbiol.* **2016**, *7*, doi:10.3389/fmicb.2016.00674.

22. Drake, H.; Ivarsson, M.; Bengtson, M.; Heim, C.; Siljeström, S.; Whitehouse, M.; Broman, C.; Belivanova, V.; Åström, M.E. Anaerobic consortia of fungi and sulfate reducing bacteria in deep granite fractures. *Nat. Commun.* **2017**, *8*, doi:10.1038/s41467-017-00094-6.

23. Stevens, T.O.; McKinley, J.P. Lithoautotrophic microbial ecosystems in deep basalt aquifers. *Science* **1995**, *270*, 450–454.

24. Lin, L.-H.; Slater, G.F.; Sherwood Lollar, B.; Lacrampe-Couloume, G.; Onstott, T.C. The yield and isotopic composition of radiolytic H_2, a potential energy source for the deep subsurface biosphere. *Geochim. Cosmochim. Acta* **2005**, *69*, 893–903.

25. Pedersen, K. Metabolic activity of subterranean microbial communities in deep granitic groundwater supplemented with methane and H_2. *ISME J.* **2012**, *7*, 839–849.

26. Lau, M.C.; Kieft, T.L.; Kuloyo, O.; Linage-Alvarez, B.; van Heerden, E.; Lindsay, M.R.; Magnabosco, C.; Wang, W.; Wiggins, J.B.; Guo, L.; et al. An oligotrophic deep-subsurface community dependent on syntrophy is dominated by sulfur-driven autotrophic denitrifiers. *Proc. Natl Acad. Sci. USA* **2016**, *113*, E7927–E7936.

27. McCollom, T.M. Abiotic methane formation during experimental serpentinization of olivine. *Proc. Natl Acad. Sci. USA* **2016**, *113*, 13965–13970.

28. McCollom, T.M. Geochemical constraints on sources of metabolic energy for chemolithoautotrophy in ultramafic-hosted deep-sea hydrothermal systems. *Astrobiology* **2007**, *7*, 933–950.

29. Anderson, R.T.; Chapelle, F.H.; Lovley, D.R. Evidence against hydrogen-based microbial ecosystems in basalt aquifers. *Science* **1998**, *281*, 976–977.

30. Gregory, S.P.; Barnett, M.J.; Field, L.P.; Milodowski, A.E. Subsurface microbial hydrogen cycling: Natural occurrence and implications for industry. *Microorganisms* **2019**, *7*, doi:10.3390/microorganisms7020053.

31. Fytikas, M.; Innocenti, F.; Kolios, N.; Manetti, P.; Mazzuoli, R.; Poli, G.; Rita, F.; Villari, L. Volcanology and petrology of volcanic products from the island of Milos and Neighbouring islets. *J. Vol. Geotherm. Res.* **1986**, *28*, 297–317.

32. Stewart, A.L.; McPhie, J. Facies architecture and Late Ploicene—Pleistocene evolution of a felsic volcanic island, Milo, Greece. *Bull. Volcanol.* **2006**, *68*, 703–726.

33. Hannington, M.D.; de Ronde, C.E.J.; Petersen, S. Sea-floor tectonics and submarine hydrothermal systems. *Econ. Geol. 100th Anniv. Vol.* **2005**, *100*, 111–142.

34. Naden, J.; Kilias, S.P.; Darbyshire, D.P.F. Active geothermal systems with entrained seawater as modern analogs for transitional volcanic-hosted massive sulphide and continental magmato-hydrothermal mineralization: The example of Milos Island, Greece. *Geology* **2005**, *33*, 541–544.

35. Alfieris, D.; Voudouris, P.; Spry, P.G. Shallow submarine epithermal Pb–Zn–Cu–Au–Ag–Te mineralization on western Milos Island, Aegean Volcanic Arc, Greece: Mineralogical, geological and geochemical constraints. *Ore Geol. Rev.* **2013**, *53*, 159–180.

36. Smith, D.J.; Naden, J.; Miles, A.-J.; Bennet, H.; Bicknell, S.H. Mass wasting events and their impact on the formation and preservation of submarine deposits. *Ore Geol. Rev*. **2018**, *7*, 143–151.

37. Hein, J.R.; Stamatakis, M.G.; Dowling, J.S. Trace metal-rich Quaternary hydrothermal manganese oxide and barite deposit, Milos Island, Greece. *Appl. Earth Sci.* **2000**, *109*, 67–76.

38. Liakopoulos, A.; Glasby, G.P.; Papavassiliou, C.T.; Boulegue, J. Nature and origin of the Vani manganese deposit, Milos, Greece: An overview. *Ore Geol. Rev.* **2001**, *18*, 181–209.

39. Chi Fru, E.; Kilias, S.; Ivarsson, M.; Rattray, J.E.; Gkika, K.; McDonald, I.; He, Q.; Broman, C. Sedimentary mechanisms of a modern banded iron formation on Milos Island, Greece. *Solid Earth* **2018**, *9*, 573–598.

40. Dando, P.R.; Hughes, J.A.; Leahy, Y.; Niven, S.J.; Taylor, L.J.; Smith, C. Gas venting from submarine hydrothermal areas around island of Milos, Hellenic Volcanic Arc. *Cont. Shelf Res.* **1995**, *15*, 913–929.

41. Kilias, S.P. Microbial-mat related structures in the Quaternary Cape Vani manganese oxide (-barite) deposit, NW Milos island-Greece. In *Microbial Mats in Siliciclastic Depositional Systems through Time*; SEPM Special Publication, Athen, Greece: 2012; Volume 101, pp. 97–110.

42. Kilias, S.P.; Detsi, K.; Godelitsas, A.; Typas, M.; Naden, J.; Marrantos, Y. Evidence of Mn-oxide biomineralization, Vani Mn deposit, Milos, Greece. In Proceedings of the Ninth Bienniela SGA Meeting, Dublin, UK, 20–23 August 2007; Andrew, C.J. Ed; Digging Deeper: Dublin, UK, 2007; pp. 1069–1072.

43. Skarpelis, N.; Koutles, T. Geology of epithermal mineralization of the NW part of Milos Island, Greece. In Proceedings of the 5th International Symposium on Eastern Mediterranean Geology, Thessaloniki, Greece, 14–20 April 2004; Chatzipetros, A., Pavlides, S., Eds.; School of Geology, Aristotelian University of Thessaloniki: Thessaloniki, Greece, 2004; pp. 1449–1452.

44. Papavassilliou, K.; Voudouris, P.; Kanellopoulos, C.; Glasby, G.; Alfieris, D.; Mitsis, I. New geochemical and mineralogical constraints on the genesis of the Vani hydrothermal manganese deposit at NW Milos island, Greece: Comparison with the Aspro Gialoudi deposit and implications for the formation of the Milos manganese mineralization. *Ore Geol.* **2017**, *80*, 594–611.

45. Chi Fru, E.; Ivarsson, M.; Kilias, S.P.; Frings, S.; Hemmingsson, C.; Broman, C.; Bengtson, S.; Chatzitheodoridis, C. Biogenicity of an early Quaternary iron formation, Milos Island, Greece. *Geobiology* **2015**, *13*, 225–244.

46. Bonfante-Fasolo, P.; Faccio, A.; Perotto, S.; Schubert, A. Correlation between chitin distribution and cell wall morphology in the mycorrhizal fungus Glomus versiforme. *Mycol. Res.* **1990**, *94*, 157–165.

47. Coleman, M.; Moore, M. Direct reduction of sulphates to sulphur dioxide for isotopic analysis. *Anal. Chem.* **1978**, *50*, 1594–1595.

48. Hall, A.J.; Boyce, A.J.; Fallick, A.E.; Hamilton, P.J. Isotopic evidence of the depositional environment of Late Proterozoic stratiform barite mineralization, Aberfeldy, Scotland. *Chem. Geol.* **1991**, *87*, 99–114.

49. Whitehouse, M.J. Multiple sulfur isotope analysis by SIMS: Evaluation of reference sulfides for $\Delta^{33}S$ with observations and a case study on determination of $\Delta^{36}S$. *Geostand. Geoanal. Res.* **2013**, *37*, doi:10.1111/j.1751-908X.2012.00188.x.

50. Heinonen, A.; Andersen, T.; Rämö, O.T.; Whitehouse, M. The source of Proterozoic anorthosite and rapakivi granite magmatism: Evidence from combined in situ Hf–O isotopes of zircon in the Ahvenisto complex, southeastern Finland. *J. Geol. Soc.* **2015**, *172*, 103–112.

51. Stern, R.A. (University of Alberta, Edmonton, Canada). Personal communication, 2019.

52. Ding, T.; Valkires, S.; Kipphardt, H.; De Bievre, P.; Taylor, P.D.P.; Gonfiantini, R.; Krouse, R. Calibrated sulfur isotope abundance ratios of three IAEA sulfur isotope reference materials and V-CDT with a reassessment of the atomic weight of sulfur. *Geochim. Cosmochim. Acta* **2001**, *65*, 2433–2437.

53. Coplen, T.B. Reporting of stable hydrogen, carbon, and oxygen isotopic abundances. *Pure Appl. Chem.* **1994**, *66*, 273–276.

54. Ivarsson, M.; Kilias, S.P.; Broman, C.; Naden, J.; Detsi, K. Fossilized microorganisms preserved as fluid inclusions in epithermal veins, Vani Mn-Ba deposit, Milos Island, Greece. In Proceedings of the XIX CBGA Congress, Thessaloniki, Greece, 23–26 September 2010; Volume 100, pp. 297–307.

55. Bodnar, R.J. Revised equation and table for determining the freezing point depression of H_2O-NaCl solutions. *Geochim. Cosmochim. Acta* **1993**, *57*, 683–684.

56. Orange, D.; Knittle, E.; Farber, D.; Williams, Q. Raman spectroscopy of crude oils and hydrocarbon fluid inclusions: A feasibility study. In *Mineral Spectroscopy: A tribute to Roger G. Burns*; Dyar, M.D., McCammon, C., Schaefer, M.W., Eds.; The Geochemical Society, Special Publications: Washington DC, USA, 1996; Volume 5, pp. 65–81.

57. Rahl, J.M.; Anderson, K.M.; Brandon, M.T.; Fassoulas, C. Raman spectroscopic carbonaceous material thermometry of low-grade metamorphic rocks: Calibration and application to tectonic exhumation in Crete, Greece. *Earth Planet. Sci. Lett.* **2005**, *240*, 339–354.

58. Lahfid, A.; Beyssac, O.; Deville, E.; Negro, F.; Chopin, C.; Goffé, B. Evolution of the Raman spectrum of carbonaceous material in low-grade metasediments of the Glarus Alps (Switzerland). *Terra Nova* **2010**, *22*, 354–360.

59. Julien, C.; Massot, M.; Baddour-Hadjean, R.; Franger, S.; Bach, S.; Pereira-Ramos, J.P. Raman spectra of birnessite manganese dioxides. *Sol. Stn. Ion.* **2003**, *159*, 345–356.

60. Frezzotti, M.L.; Tecce, F.; Casagli, A. Raman spectroscopy for fluid inclusion analysis. *J. Geochem. Expl.* **2012**, *112*, 1–20.

61. Downs, R.T. The RRUFF Project: An integrated study of the chemistry, crystallography, Raman and infrared spectroscopy of minerals. In Proceedings of the Program and Abstracts of the 19th General Meeting of the International Mineralogical Association, Kobe, Japan, 23–28 July 2006; pp. 3–13.

62. Lehmann, M.F.; Bernasconi, S.M.; Barbieri, A.; McKenzie, J.A. Preservation of organic matter and alteration of its carbon and nitrogen isotope composition during simulated and in situ early sedimentary diagenesis. *Geochim. Cosmochem. Acta* **2002**, *66*, 3572–3584.

63. Paytan, A.; Martinez-Ruiz, F.; Eagle, M.; Ivy, A.; Wankel, S.D. Using sulfur isotopes to elucidate the origin of barite associated with high organic matter accumulation events in marine sediments. In *Sulfur Biogeochemistry—Past and Present*; Amend, J.P., Edwards, K.J., Lyons, T.W., Eds.; Geological Society of America Special Paper: Boulder, CO, USA, 2004; Volume 379, pp. 151–160.

64. Paytan, A.; Kastner, M.; Campbell, D.; Thiemens, M.H. Sulfur isotopic composition of Cenozoic seawater sulfate. *Science* **1998**, *282*, 1459–1462.

65. Turchyn, A.V.; Schrag, D.P. Oxygen isotope constraints on the sulphur cycle over the past 10 million years. *Science* **2004**, *303*, 2004–2007.

66. Turchyn, A.V.; Schrag, D.P. Cenozoic evolution of the sulphur cycle: Insight from oxygen isotopes in marine sulfate. *Earth Planet. Sci. Lett.* **2006**, *241*, 763–779.

67. Aharon, P.; Fu, B. Microbial sulfate reduction rates and sulphur and oxygen isotope fractionations at oil and gas seeps in deepwater Gulf of Mexico. *Geochim. Cosmochim Acta* **2000**, *64*, 233–246.

68. Kilias, S.; Naden, J.; Cheliotis, I.; Shepherd, T.J.; Constandinidous, H.; Crossing, J.; Simos, J. Epithermal gold mineralization in the active Aegean Volcanic Arc: The Profitis Ilias deposit, Milos Island, Greece. *Miner. Depos.* **2001**, *36*, 32–44.

69. Bakker, R.J. Package FLUIDS 1. Computer programs for analysis of fluid inclusion data and for modelling bulk fluid properties. *Chem. Geol.* **2003**, *194*, 3–23.

70. Papanikolaou, D.; Lekkas, E.; Syskakis, D. Tectonic analysis of the geothermal field of Milos Island. *Bull. Geol. Soc. Greece* **1990**, *24*, 27–46.

71. Peter, J.M.; Peltonen, P.; Scott, S.D.; Simoneit, B.R.T.; Kawka, O.E. [14]C ages of hydrothermal petroleum and carbonate in Guaymas Basin, Gulf of California: Implications for oil generation, expulsion, and migration. *Geology* **1991**, *19*, 253–256.

72. Simoneit, B.R. Hydrothermal petroleum: Genesis, migration, and deposition in Guaymas Basin, Gulf of California. *Can. J. Earth Sci.* **1985**, *22*, 1919–1929.

73.   Simoneit, B.R.T.; Leif, R.N.; Sturz, A.A.; Sturdivant, A.E.; Gieskes, J.M. Geochemistry of shallow sediments in Guaymas Basin, Gulf of California: Hydrothermal gas and oil migration and effects of mineralogy. *Org. Geochem.* **1992**, *18*, 765–784.

74.   Simoneit, B.R. Hydrothermal Petroleum. In *Hydrocarbons, Oils and Lipids: Diversity, Origin, Chemistry and Fate*; Springer: Berlin, Germany, 2018; pp. 1–35.

75.   Yamanaka, T.; Ishibashi, J.; Hashimoto, J. Organic geochemistry of hydrothermal petroleum generated in the submarine Wakamiko caldera, southern Kyushu, Japan. *Org. Geochem.* **2000**, *31*, 1117–1132.

76.   Teske, A.; De Beer, D.; McKay, L.J.; Tivey, M.K.; Biddle, J.F.; Hoer, D.; Lloyd, K.G.; Lever, M.A.; Røy, H.; Albert, D.B.; et al. The Guaymas Basin hiking guide to hydrothermal mounds, chimneys, and microbial mats: Complex seafloor expressions of subsurface hydrothermal circulation. *Front. Microbial.* **2016**, *7*, 75.

77.   Daskalopoulou, K.; Gagliano, A.L.; Calabrese, S.; Longo, M.; Hantzis, K.; Kyriakopoulos, K.; D'Alessandro, W. Gas geochemistry and CO_2 output estimation at the island of Milos, Greece. *J. Volcanol. Geotherm. Res.* **2018**, *365*, 13–22.

78.   Feng, D.; Roberts, H.H. Geochemical characteristics of the barite deposits at cold seeps from the northern Gulf of Mexico continental slope. *Earth Planet. Sci. Lett.* **2011**, *309*, 89–99.

79.   Aquilina, L.; Pauwels, H.; Genter, A.; Fouillac, C. Water-rock interaction processes in the Triassic sandstone and the granitic basement of the Rhine Graben: Geochemical investigation of a geothermal reservoir. *Geochim. Cosmochim. Acta* **1997**, *61*, 4281–4295.

80.   Richards, J.P. A shake-up in the porphyry world? *Econ. Geol.* **2018**, *118*, 1225–1233.

81.   Bodnar, R.J. Introduction to aqueous-electrolyte fluid inclusions. In *Fluid Inclusions: Analysis and Interpretation*; Samson, I., Anderson, A., Marshall, D., Eds.; Mineralogical Association of Canada: Quebec City, QC, Cananda, 2003; Volume 32, pp. 81–99.

82.   Ehrlich, H.L. *Geomicrobiology*; Marcel Dekker: New York, NY, USA, 2002.

83.   Puente-Sánchez, F.; Arce-Rodríguez, A.; Oggerind, M.; García-Villadangosa, M.; Moreno-Paza, M.; Blancoa, Y.; Rodríguez, N.; Birde, L.; Lincolne, S.A.; Tornos, F.; et al. Viable cyanobacteria in the deep continental subsurface. *Proc. Natl. Acad. Sci. USA* **2018**, *115*, 10702–10707.

84.   Salman, V.; Bailey, J.V.; Teske, A. Phylogenetic and morphologic complexity of giant sulphur bacteria. *Antonie van Leeuwenhoek* **2013**, *104*, 169–186.

85.   Schulz, H.N.; Jørgensen, B.B. Big Bacteria. *Annu. Rev. Microbiol.* **2001**, *55*, 105–137.

86.   Cunningham, J.A.; Thomas, C.-W.; Bengtson, S.; Marone, F.; Stampanoni, M.; Turner, F.R.; Bailey, J.V.; Raff, R.A.; Raff, E.C.; Donoghue, P.C.J. Experimental taphonomy of giant Sulphur bacteria: Implications for the interpretation of the embryo-like Ediacaran Doushantuo fossils. *Proc. R. Soc. B.* **2012**, *279*, 1857–1864.

87.   Carrera, M.; Zandomeni, R.O.; Fitzgibbon, J.; Sagripanti, J.-L. Difference between the spore sizes of *Bacillus anthracis* and other *Bacillus* species. *J. Appl. Microbiol.* **2007**, *102*, 303–312.

88.   Perretto, R.; Bettini, V.; Favaron, F.; Alghisi, P.; Bonfante, P. Polygalacturonase activity and location in arbuscular mycorrhizal roots of Allium porrum L. *Mycorrhiza* **1995**, *5*, 157–163.

89.   Fife, D.J.; Bruhn, D.F.; Miller, K.S.; Stoner, D.L. Evaluation of a fluorescent lectin-based staining technique for some acidophilic mining bacteria. *Appl. Environ. Microbiol.* **2000**, *66*, 2208–2210.

90.   Montgomery, M.T.; Welschmeyer, N.A.; Kirchman, D.L. A simple assay for chitin: Application to sediment trap samples from the subarctic Pacific. *Mar. Ecol. Prog. Ser.* **1990**, *64*, 301–308.

91.   Rawat, R.; Rawat, S. Colorless sulfur oxidizing bacteria from diverse habitats. *Adv. Appl. Sci. Res.* **2015**, *6*, 230–235.

92.   Wohl, D.L.; McArthur, J.V. Aquatic Actinomycete-fungal interactions and their effects on organic matter decomposition: A microcosm study. *Microbial. Ecol.* **2001**, *42*, 446–457.

93.   Orsi, W.D.; Edgcomb, V.D.; Chrsitman, G.D.; Biddle, J.F. Gene expression in the deep biosphere. *Nature* **2013**, *499*, 205–208.

94.   Orsi, W.D.; Biddle, J.F.; Edgcomb, V.D. Deep sequencing of subseafloor eukaryotic rRNA reveals active fungi across marine subsurface provinces. *PLoS ONE* **2013**, *8*, 1–10.

95.   Maheshwani, R.; Bharadwaj, G.; Bhat, M.K. Thermophilic fungi: Their physiology and enzymes. *Microbiol. Mol. Rev.* **2000**, *64*, 461–488.

96.   Ivarsson, M.; Broman, C.; Lindblom, S.; Holm, N.G. Fluid inclusions as a tool to constrain the preservation conditions of sub-seafloor cryptoendoliths. *Planet. Space Sci.* **2009**, *57*, 477–490.

97.   Tebo, B.M.; Johnson, H.A.; McCarthy, J.K.; Templeton, A.S. Geomicrobiology of manganese (II) oxidation. *Trends Microbiol.* **2005**, *13*, 421–428.

98. Ehrlich, H.L.; Newman, D.K. Geomicrobiology of manganese. In *Geomicrobiology*; Ehrlich, H.L., Newman, D.K. Eds.; CRC Press: Boca Raton, FL, USA, 2009; pp. 347–420.

99. Hansel, C.M.; Zeiner, C.A.; Santelli, C.M.; Webb, S.M. Mn (II) oxidation by anascomycete fungus is linked to superoxide production during asexual reproduction. *Proc. Natl. Acad. Sci. USA* **2012**, *109*, 12621–12625.

100. Francis, C.A.; Tebo, B.M. Enzymatic manganese (II) oxidation by metabolically dormant spores of diverse *Bacillus* species. *Appl. Environ. Microbiol.* **2002**, *68*, 874–880.

101. Santelli, C.M.; Pfister, D.H.; Lazarus, D.; Sun, L.; Burgos, W.D.; Hansel, C.M. Promotion of Mn (II) oxidation and remediation of coal mine drainage in passive treatment systems by diverse fungal and bacterial communities. *Appl. Environ. Microbiol.* **2010**, *76*, 4871–4875.

102. Hansel, C.M.; Francis, C.A. Coupled photochemical and enzymatic Mn (II) oxidation pathways of a planktonic *Roseobacter*-like bacterium. *Appl. Environ. Microbiol.* **2006**, *72*, 3543–3549.

103. Dubessy, J.; Pagel, M.; Beny, J.-M.; Christensen, H.; Hickel, B.; Kosztolanyi, C.; Poty, B. Radiolysis evidence by H_2-O_2 and H_2-bearing fluid inclusions in three uranium deposits. *Geochim. Cosmochim. Acta* **1988**, *52*, 1155–1167.

104. Li, J.; Chou, I.-M. Hydrogen in silicate melt inclusions in quartz from granite detected with Raman spectroscopy. *J. Ram. Spectrophotometer* **2015**, *46*, 983–986.

105. Haruta, M.; Yamada, N.; Kobayashi, T.; Iijima, S. Gold catalysts prepared by coprecipitation for low-temperature oxidation of hydrogen and carbon monoxide. *J. Catal.* **1989**, *115*, 301–309.

106. Torres Sanchez, R.M.; Ueda, A.; Tanaka, K.; Haruta, M. Selective oxidation of CO in hydrogen over gold supported on manganese oxides. *J. Catal.* **1997**, *168*, 125–127.

107. Botz, R.; Stüben, D.; Winckler, G.; Bayer, R.; Schmitt, M.; Faber, E. Hydrothermal gases offshore Milos Island, Greece. *Chem. Geol.* **1996**, *130*, 161–173.

108. Daskalopoulou, K.; Calabrese, S.; Grassa, F.; Kyriakopoulos, K.; Parello, F.; Tassi, F.; D'Alessandro, W. Origin of methane and light hydrocarbons in natural fluid emissions: A key study from Greece. *Chem. Geol.* **2018**, *479*, 286–301.

109. Sherwood Lollar, B.; Lacrampe-Couloume, G.; Slater, G.F.; Ward, J.; Moser, D.P.; Gihring, T.M.; Lin, L.-H.; Onstott, T.C. Unravelling abiogenic and biogenic sources of methane in the Earth's deep subsurface. *Chem. Geol.* **2006**, *226*, 328–339.

110. Nandi, R.; Sengupta, S. Microbial production of hydrogen: An overview. *Crit. Rev. Microbiol.* **1998**, *24*, 61–84.

111. Gray, C.T.; Gest, H. Biological formation of molecular hydrogen. *Science* **1965**, *148*, 186–192.

112. Horner, D.S.; Foster, P.G.; Embley, T.M. Iron hydrogenases and the evolution of anaerobic eukaryotes. *Mol. Biol. Evol.* **2000**, *17*, 1695–1709.

113. Thorsen, M.S. Abundance and biomass of the gut-living microorganisms (bacteria, protozoa and fungi) in the irregular sea urchin Echinocardium cordatum (Spatangoida: Echinodermata). *Mar. Ecol.* **1999**, *133*, 353–360.

114. Mackie, R.I.; Rycyk, M.; Ruemmler, R.L.; Aminov, R.I.; Wikelski, M. Biochemical and microbiological evidence for fermentative digestion in free-living land iguanas (Conolophus pallidus) and marine ignuanas (Amblyrhynchus cristatus) on the Galapagos archipelago. *Phys. Biochem. Zool.* **2004**, *77*, 127–138.

115. Lockhart, R.J.; Van Dyke, M.I.; Beadle, I.R.; Humphryes, P.; McCarthy, A.J. Molecular biological detection of anaerobic gut fungi (Neocallimastigales) from landfill sites. *Appl. Environ. Microbiol.* **2006**, *72*, 5659–5661.

116. Wurzbacher, C.; Warthmann, N.; Bourne, E.; Attermeyer, K.; Allgaier, M.; Powell, J.R.; Detering, H.; Mbedi, S.; Grossart, H.-P.; Monaghan, M.T. High habitat-specificity in fungal communities in oligo-mesotrophic, temperate Lake Stechlin (North-East Germany). *MycoKeys* **2016**, *16*, 17–44.

117. Mohamed, D.J.; Martiny, J.B. Patterns of fungal diversity and composition along a salinity gradient. *ISME J.* **2011**, *5*, 379–388.

118. Picard, K.T. Coastal marine habitats harbour novel early-diverging fungal diversity. *Fungal Ecol.* **2017**, *25*, 1–13.

119. Müller, M.; Mentel, M.; van Hellemod, J.J.; Henze, K.; Woehle, C.; Goild, S.B.; Yu, R.-Y.; van der Giezen, M.; Tielens, A.G.M.; Martin, W.F. Biocemistry and evolution of anaerobic energy metabolism in eukaryotes. *Microbiol. Mol. Biol. Rev.* **2012**, *76*, 444–495.

120. Hjorth, K.; Goldberg, A.V.; Tsaousis, A.D.; Hirt, R.P.; Embley, T.M. Diversity and reductive evolution of mitochondria among microbial eukaryotes. *Phil. Trans. R. Soc. B Biol. Sci.* **2010**, *365*, 713–727.

121. Embley, T.M.; O'Neill, A.H.; Thomsson, E.; Pedersen, K. Characterisation of yeasts isolated from deep igneous rock aquifers of the Fennoscandian shield. *Microb. Ecol.* **2003**, *46*, 416–428.

122. Baranenko, V.I.; Kirov, V.S. Solubility of hydrogen in water in a broad temperature and pressure range. *Sov. At. Energy* **1989**, *66*, 30–34.